Theory of tunneling conductance of anomalous Rashba metal/superconductor junctions

Toshiyuki Fukumoto, Katsuhisa Taguchi, Shingo Kobayashi, and Yukio Tanaka
Department of Applied Physics, Nagoya University, Nagoya 464-8603, Japan
(Received 20 August 2015; published 27 October 2015)

We theoretically study charge conductance in anomalous Rashba metal (ARM)/superconductor junctions for various types of pairing symmetries in a superconductor. The exotic state dubbed ARM, where one of the spin-resolved Fermi surfaces is absent, is realized when the chemical potential is tuned both in the presence of Rashba spin-orbit interaction (RSOI) and an exchange field. Although a fully polarized ferromagnet metal (FPFM) is also a system in which the electron's spin degrees of freedom are reduced by half, the electrons in an ARM have features that are distinct from those in a FPFM. For the ARM/spin-singlet superconductor junctions, the obtained tunneling conductance within the bulk energy gap is enhanced with the increase in magnitude of the RSOI. In particular, in ARM/d_{xy}-wave superconductor junctions, the zero-bias conductance peak is enhanced due to the presence of the RSOI. For ARM/p_x-wave superconductor junctions, the condition of the existence of the zero-bias conductance peak is significantly sensitive to the direction of the $\boldsymbol{d}$ vector of the p_x-wave superconductor. Furthermore, the obtained conductance in ARM/chiral p-wave superconductor junctions shows different behaviors as compared to those in ARM/helical p-wave superconductor junctions. This feature serves as a guide to determine the spin structure of a Cooper pair in the spin-triplet superconductor Sr_2RuO_4.

DOI: 10.1103/PhysRevB.92.144514 PACS number(s): 74.55.+v, 74.25.F−

I. INTRODUCTION

Determination of the pairing symmetry of a Cooper pair has been an important issue in the field of superconductivity. In this regard, tunneling spectroscopy is known to be useful. In unconventional superconductor junctions, a zero-bias conductance peak (ZBCP) due to the surface Andreev bound state (SABS) is observed [1–4], where the pair potential changes its sign on the Fermi surface [4,5]. Actually, the presence of a sharp ZBCP in the tunneling conductance in N/S junctions supports d-wave symmetry in a cuprate [5,6]. In addition, a broad ZBCP observed in Sr_2RuO_4 junctions [7] is consistent with the SABS with linear dispersion, such as chiral p-wave pairing [8–11]. Moreover, the tunneling spectroscopy in ferromagnet/superconductor (FM/S) junctions has also been studied up to now. For a spin-singlet superconductor, the magnitude of the tunneling conductance with the inner gap regime is suppressed [12]. In addition, in the case of a fully polarized ferromagnet metal (FPFM), the inner gap conductance is completely suppressed [13–17]. On the other hand, for the spin-triplet p-wave case [17–19], the resulting conductance depends on the direction of the $\boldsymbol{d}$ vector, which is perpendicular to the direction of the spin of a spin-triplet Cooper pair.

Recently, the role of spin-orbit interactions in tunneling spectroscopy in a superconductor has attracted much attention, potentially opening up a new direction for superconducting spintronics. One of the properties of the Rashba spin-orbit interaction (RSOI) is that it splits the Fermi surface depending on the spin degrees of freedom, where the relative direction of the spin and momentum are locked due to the RSOI in each Fermi surface [20–22]. This unique property in a metal or doped semiconductor has attracted much attention in superconducting junctions as well as in the field of spintronics, since the direction of spin can be manipulated by the control of the RSOI [23–27]. For example, RSOI-dependent charge transport has been studied in a two-dimensional electron gas (2DEG) with RSOI/s-wave superconductor junctions [28–30].

In the 2DEG, introducing an exchange field or applying an external magnetic field, a gap opens at the crossing point of two split bands by the RSOI [31]. If we set the chemical potential in between the induced energy gap by manipulating the exchange field, the inner Fermi surface disappears. Thus, we can imagine novel quantum phenomena in the present system since only one of the Kramers doublets exists. In the following, we call this state an anomalous Rashba metal (ARM). The aim of this paper is to study the tunneling spectroscopy in ARM/S junctions. A unique feature of the tunneling conductance is expected in ARM/S junctions due to the reduction in spin degrees of freedom and the unique spin configuration of the ARM. Furthermore, it would be interesting to compare the ARM with the FPFM, both of which host half of the spin degrees of freedom; however, as shown in Figs. 1(a) and 1(b), the spin textures in the band basis behave differently from each other. This difference gives a distinctive signature to each superconductor junction.

Furthermore, it is known that the surface state of topological insulators (TIs) [32] also has half of the spin degrees of freedom and a unique spin texture [33], which is the so-called helical metal. However, whereas TIs preserve time-reversal symmetry, ARMs break it. Thus, ARMs are fundamentally different from TIs. For superconductor junctions via a helical metal, there have been several studies on the surface of TIs, and the unique feature of charge transport in the systems has been reported [34–38]. While the properties of charge transport in ARM/S junctions are naturally expected to be anomalous, similar to helical metal, they have not been revealed yet.

In this paper, we theoretically study the tunneling conductance in the ARM/S junctions by solving the Bogoliubov–de Gennes (BdG) equation within the quasiclassical approximation for several pairing symmetries: s-wave, p-wave, d-wave, chiral p-wave, helical p-wave, and chiral d-wave pairings. Among them, we reveal a qualitative difference between the N, the FPFM, and the ARM in superconducting junctions. For ARM/s-wave superconductor junctions, the

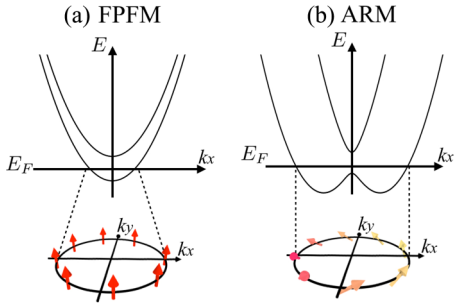

FIG. 1. (Color online) Schematic illustration of the energy dispersion and the spin configuration on the Fermi surface in (a) an FPFM and (b) ARM. We assume that the exchange field is along the z axis. In addition, the RSOI $\lambda(\boldsymbol{\sigma} \times \boldsymbol{k}) \cdot \boldsymbol{z}$ is considered in the ARM. In the FPFM, the spin directions on the Fermi surface point to the z direction, whereas, in the ARM, they rotate along the Fermi surface and tilt to the z axis.

magnitude of the inner gap conductance is enhanced as the RSOI increases; this behavior is clearly different from that of FPFM/s-wave superconductor junctions. In a similar manner, for ARM/d_{xy}-wave superconductor junctions, the RSOI retains the ZBCP. This contrasts sharply with the suppression of the ZBCP in FPFM/d_{xy}-wave superconductor junctions [13–15]. In addition, we find that, for ARM/p_x-wave superconductor junctions, the magnitude of the ZBCP depends significantly on the direction of the $\boldsymbol{d}$ vector in the p_x-wave superconductor. In our setup, the obtained ZBCP remains only when the y component of the $\boldsymbol{d}$ vector is nonzero. This $\boldsymbol{d}$-vector dependence comes from the RSOI; thus, this feature is peculiar to ARM/p_x-wave superconductor junctions. We also show that the presence or absence of the ZBCP is related to a topological number in a p_x-wave superconductor. When the symmetry of S is a chiral p-wave, helical p-wave, and chiral d-wave pairing, the pairing symmetries show qualitatively different line shapes of the tunneling conductance.

The organization of this paper is as follows. In Sec. II, we explain our model and give a formulation of the tunneling conductance. In Sec. III A, the tunneling conductance of the ARM/s-wave superconductor junction is calculated. In Sec. III B, the tunneling conductance of the ARM/d_{xy}-wave superconductor junction is shown. We discuss the relevance to the tunneling spectroscopy of the LSMO/YBCO junction. The calculation for the ARM/p_x-wave superconductor junction is shown in Sec. III C. We interpret the obtained results using a chiral operator based on the topology of the Hamiltonian. In Sec. IV, we show the tunneling conductance for an ARM/chiral p-wave superconductor, an ARM/chiral d-wave superconductor, and ARM/helical p-wave superconductor junctions. In Sec. V, we present our conclusions.

II. FORMULATION FOR THE TUNNELING CONDUCTANCE

Let us consider a two-dimensional ARM/insulator/superconductor junction in the ballistic limit. We assume that the ARM/S interface is located at $x = 0$ (along the y axis). The interface has an infinitely narrow insulating barrier described by the δ function. In this section, a formulation of tunneling conductance in two-dimensional ARM/S junctions is shown.

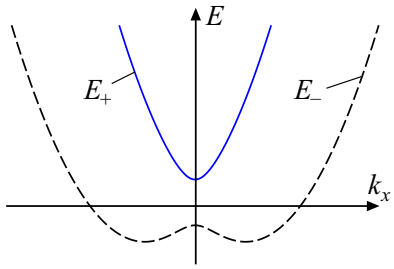

FIG. 2. (Color online) The energy spectrum of the ARM. The eigenvalues are given by $E_\pm = \xi_{\boldsymbol{k}} \pm \sqrt{H^2 + (\lambda k)^2}$.

We start from the BdG Hamiltonian including both the exchange field and the RSOI as shown below,

$$\bar{H} = \begin{bmatrix} \hat{H}(\boldsymbol{k}) & \hat{\Delta}(\boldsymbol{k})\theta(x) \\ \hat{\Delta}(\boldsymbol{k})^\dagger\theta(x) & -\hat{H}(-\boldsymbol{k})^* \end{bmatrix}, \tag{1}$$

$$\hat{H}(\boldsymbol{k}) = \begin{bmatrix} \xi_{\boldsymbol{k}} + H\theta(-x) + V_0\delta(x) & i\lambda k_-\theta(-x) \\ -i\lambda k_+\theta(-x) & \xi_{\boldsymbol{k}} - H\theta(-x) + V_0\delta(x) \end{bmatrix}, \tag{2}$$

$$\hat{\Delta}(\boldsymbol{k}) = i\hat{\sigma}_y[d_0(\boldsymbol{k})\hat{\sigma}_0 + \boldsymbol{d}(\boldsymbol{k})\hat{\boldsymbol{\sigma}}], \tag{3}$$

with $k_\pm = k_x \pm ik_y$, $\xi_{\boldsymbol{k}} = \frac{k^2}{2m} - \mu_N\theta(-x) - \mu_S\theta(x)$, and $\hbar = 1$. $\hat{\Delta}(\boldsymbol{k})$, μ_N (μ_S), $\lambda(>0)$, $H(>0)$, and $\theta(x)$ are the pair potential, the chemical potential in the metal (superconductor), the amplitude of RSOI, the exchange field, and the step function, respectively. In Eq. (3), $d_0(\boldsymbol{k})$ denotes the pair potential in the spin-singlet superconductor, and $\boldsymbol{d}(\boldsymbol{k})$ $[=(d_x(\boldsymbol{k}),d_y(\boldsymbol{k}),d_z(\boldsymbol{k}))]$ is the $\boldsymbol{d}$ vector of spin-triplet superconductor. When the spin-singlet (spin-triplet) superconductor is considered in $x > 0$, we choose $\boldsymbol{d} = \boldsymbol{0}$ ($d_0 = 0$). Here, we assume that the exchange field is parallel to the z axis. In addition, the z component of the RSOI $\lambda(\hat{\boldsymbol{\sigma}} \times \boldsymbol{k}) \cdot \boldsymbol{z}$ is considered, where σ_i ($i = 0,x,y,z$) are the identity matrix and the Pauli matrix in spin space. The energy spectrum of the ARM is given by $E_\pm = \xi_{\boldsymbol{k}} \pm \sqrt{H^2 + (\lambda k)^2}$ (see Fig. 2). It should be made clear that our Hamiltonian is distinct from an ARM/spin-singlet s-wave superconductor hybrid system in which the pair potential is induced in the ARM. In that case, the ARM hosts a chiral Majorana mode as an edge state [39–45]. To calculate the tunneling conductance of the ARM/S junctions, we choose $|\mu| < H$ in the following calculation. The Fermi momentum for the outer (inner) Fermi surface $k_{1(2)}$ in the ARM is given as follows:

$$k_{1(2)} = \sqrt{2m(\mu_N + m\lambda^2 + (-)\sqrt{(m\lambda^2)^2 + 2m\lambda^2\mu_N + H^2})}. \tag{4}$$

Here, k_2 is a purely imaginary number and represents an evanescent wave because of the absence of the inner Fermi surface (FS). To specify this, we define a real number κ_2 ($i\kappa_2 = k_2$),

$$\kappa_2 = \sqrt{2m(\sqrt{(m\lambda^2)^2 + 2m\lambda^2\mu_N + H^2} - \mu_N - m\lambda^2)}. \tag{5}$$

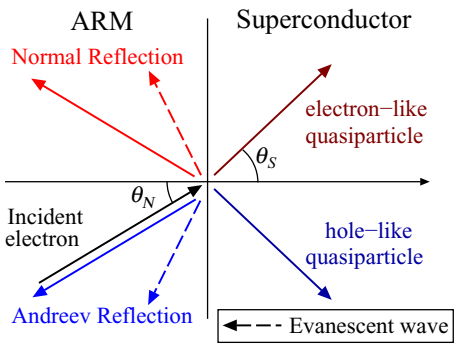

FIG. 3. (Color online) Schematic illustration of the scattering process. θ_N is an incident angle of k_1 with respect to the interface normal. θ_S denotes the direction of motions of quasiparticles in S measured from the interface normal.

From Eq. (5), the x component of κ_2 is given by

$$\kappa_{2x} = \sqrt{(\kappa_2)^2 + (k_y)^2}. \tag{6}$$

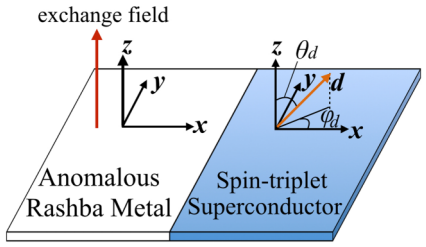

FIG. 4. (Color online) Schematic illustration of an ARM/p-wave superconductor junction. The exchange field is parallel to z axis.

In the superconductor ($x > 0$), the Fermi momentum k_S can be denoted by $k_S \approx \sqrt{2m\mu_S}$ in the quasiclassical approximation. In addition, the y component of all momenta satisfies

$$k_y = k_1 \sin\theta_N = k_S \sin\theta_S, \tag{7}$$

because a momentum parallel to the interface is conserved when we assume a flat interface.

First, we introduce a wave function in the ARM. As shown in Fig. 3, the wave function $\psi(x,y)$ in the ARM is represented by using eigenfunctions of the Hamiltonian,

$$\psi(x>0,y) = e^{ik_y y}\left(e^{ik_1\cos\theta_N x}\begin{bmatrix} s \\ 1 \\ 0 \\ 0 \end{bmatrix} + r_1 e^{-ik_1\cos\theta_N x}\begin{bmatrix} s^* \\ 1 \\ 0 \\ 0 \end{bmatrix} + a_1 e^{ik_1\cos\theta_N x}\begin{bmatrix} 0 \\ 0 \\ -s^* \\ 1 \end{bmatrix} + r_2 e^{\kappa_{2x}x}\begin{bmatrix} t_e \\ 1 \\ 0 \\ 0 \end{bmatrix} + a_2 e^{\kappa_{2x}x}\begin{bmatrix} 0 \\ 0 \\ t_h \\ 1 \end{bmatrix}\right), \tag{8}$$

$$s = -\frac{i\lambda k_1 e^{-i\theta_N}}{\xi_{k_1} + H}, \tag{9}$$

$$t_e = -\frac{\lambda(\kappa_{2x} + k_y)}{\xi_{i\kappa_2} + H}, \tag{10}$$

$$t_h = \frac{\lambda(-\kappa_{2x} + k_y)}{\xi_{i\kappa_2} + H}, \tag{11}$$

where r_1 and r_2 (a_1 and a_2) are normal (Andreev) reflection coefficients and θ_N is an injection angle of k_1 measured from the normal to the interface (see Fig. 3). In addition, we assume $\mu_S \pm \Delta_0 \approx \mu_S$ in the quasiclassical approximation. An injected electron cannot transmit into the superconductor for $\theta_N > \arcsin(\frac{k_S}{k_1})$ ($\equiv\theta_C$). Next, we calculate a wave function in the superconductors. With the magnitude of the pair potential Δ_0, the pair potential matrices for spin-singlet and spin-triplet superconductors are given by

$$\hat{\Delta}(\boldsymbol{k}) = \begin{cases} \begin{bmatrix} 0 & d_0(\boldsymbol{k}) \\ -d_0(\boldsymbol{k}) & 0 \end{bmatrix} & \text{(spin-singlet pair)}, \\ \begin{bmatrix} -d_x(\boldsymbol{k}) + id_y(\boldsymbol{k}) & d_z(\boldsymbol{k}) \\ d_z(\boldsymbol{k}) & d_x(\boldsymbol{k}) + id_y(\boldsymbol{k}) \end{bmatrix} & \text{(spin-triplet pair)}. \end{cases} \tag{12}$$

In Eq. (12), $d_0(\boldsymbol{k})$ is defined as $d_0(\boldsymbol{k}) \equiv \Delta_0 f_{\theta_S}$, where f_{θ_S} denotes the momentum dependence of the pair potential on the Fermi surface in spin-singlet superconductor. The direction of the $\boldsymbol{d}$ vector is denoted by the polar angle θ_d and the azimuthal angle ϕ_d in Fig. 4. The $\boldsymbol{d}$ vector for the p_x-wave, p_y-wave, or chiral p-wave superconductor is given by

$$\boldsymbol{d} = (d_x, d_y, d_z) = \Delta_0 g_{\theta_S}(\sin\theta_d\cos\phi_d, \sin\theta_d\sin\phi_d, \cos\theta_d). \tag{13}$$

In addition, we assume that the $\boldsymbol{d}$ vector for the helical p-wave superconductor is given by

$$\boldsymbol{d} = \Delta_0\big(w_{1\theta_S}, w_{2\theta_S}, 0\big). \tag{14}$$

Similar to f_{θ_S}, g_{θ_S} and $w_{i\theta_S}$ ($i = 1,2$) represent the momentum dependence of the pair potential on the Fermi surface in spin-triplet superconductors. The explicit forms of f_{θ_S}, g_{θ_S}, and $w_{i\theta_S}$ ($i = 1,2$) are given in Secs. III and IV. The wave functions in the spin-singlet and spin-triplet superconductors are given as follows:

(i) Spin-singlet superconductor,

$$\psi(x,y) = e^{ik_y y}\left(s_1 e^{ik_{\rm FS}\cos\theta_S x}\begin{bmatrix}1\\0\\0\\\Gamma_+\end{bmatrix} + s_2 e^{ik_{\rm FS}\cos\theta_S x}\begin{bmatrix}0\\1\\-\Gamma_+\\0\end{bmatrix} + s_3 e^{-ik_{\rm FS}\cos\theta_S x}\begin{bmatrix}0\\-\tilde{\Gamma}_-\\1\\0\end{bmatrix} + s_4 e^{-ik_{\rm FS}\cos\theta_S x}\begin{bmatrix}\tilde{\Gamma}_-\\0\\0\\1\end{bmatrix}\right), \tag{15}$$

$$\Gamma_+ = \frac{\Delta_0 f^*_{\theta_S}}{E+\sqrt{E^2-\Delta_0^2\left|f_{\theta_S}\right|^2}}, \tag{16}$$

$$\tilde{\Gamma}_- = \frac{\Delta_0 f_{\pi-\theta_S}}{E+\sqrt{E^2-\Delta_0^2\left|f_{\pi-\theta_S}\right|^2}}. \tag{17}$$

(ii) p_x-wave, p_y-wave, and chiral p-wave superconductors,

$$\psi(x,y) = e^{ik_y y}\left(s_1 e^{ik_{\rm FS}\cos\theta_S x}\begin{bmatrix}-B\\\cos\theta_d\\\Gamma_+\\0\end{bmatrix} + s_2 e^{ik_{\rm FS}\cos\theta_S x}\begin{bmatrix}\cos\theta_d\\B^*\\0\\\Gamma_+\end{bmatrix} + s_3 e^{-ik_{\rm FS}\cos\theta_S x}\begin{bmatrix}\tilde{\Gamma}_-\\0\\-B^*\\\cos\theta_d\end{bmatrix} + s_4 e^{-ik_{\rm FS}\cos\theta_S x}\begin{bmatrix}0\\\tilde{\Gamma}_-\\\cos\theta_d\\B\end{bmatrix}\right), \tag{18}$$

$$B = \sin\theta_d\cos\phi_d + i\sin\theta_d\sin\phi_d, \tag{19}$$

$$\Gamma_+ = \frac{\Delta_0 g^*_{\theta_S}}{E+\sqrt{E^2-\Delta_0^2\left|g_{\theta_S}\right|^2}}, \tag{20}$$

$$\tilde{\Gamma}_- = \frac{\Delta_0 g_{\pi-\theta_S}}{E+\sqrt{E^2-\Delta_0^2|g_{\pi-\theta_S}|^2}}. \tag{21}$$

(iii) Helical p-wave superconductor,

$$\psi(x,y) = e^{ik_y y}\left(s_1 e^{ik_{\rm FS}\cos\theta_S x}\begin{bmatrix}1\\0\\-\Gamma_{1+}+i\Gamma_{2+}\\0\end{bmatrix} + s_2 e^{ik_{\rm FS}\cos\theta_S x}\begin{bmatrix}0\\-1\\0\\\Gamma_{1+}+i\Gamma_{2+}\end{bmatrix} + s_3 e^{-ik_{\rm FS}\cos\theta_S x}\begin{bmatrix}-(\tilde{\Gamma}_{1-}+i\tilde{\Gamma}_{2-})\\0\\1\\0\end{bmatrix} + s_4 e^{-ik_{\rm FS}\cos\theta_S x}\begin{bmatrix}0\\\tilde{\Gamma}_{1-}+i\tilde{\Gamma}_{2-}\\0\\1\end{bmatrix}\right), \tag{22}$$

$$\Gamma_{j+} = \frac{\Delta_0 w^*_{j\theta_S}}{E+\sqrt{E^2-\Delta_0^2\left|w_{j\theta_S}\right|^2}}, \tag{23}$$

$$\tilde{\Gamma}_{j-} = \frac{\Delta_0 w_{j\pi-\theta_S}}{E+\sqrt{E^2-\Delta_0^2\left|w_{j\pi-\theta_S}\right|^2}}. \tag{24}$$

In the above, s_l ($l = 1,2,3,4$) denotes the transmission coefficients and $j = 1,2$. θ_S is the angle of the momentum k_S with respect to the interface normal (see Fig. 3). Since we assume that the wave function in the junction is continuous at the interface, the boundary conditions are given as follows:

$$\psi(+0,y) - \psi(-0,y) = 0, \tag{25}$$

$$\bar{v}_x[\psi(+0,y) - \psi(-0,y)] = \frac{1}{mi}2mV_0\hat{\sigma}_0\hat{\tau}_z\psi(0,y), \tag{26}$$

where $\hat{\sigma}_i$ ($\hat{\tau}_i$) ($i = 0,x,y,z$) are the identity matrix and the Pauli matrices in spin (Nambu) space. In Eq. (26), the velocity operator in the x direction $\bar{v}_x$ is defined by [22]

$$\bar{v}_x = \frac{\partial\bar{H}}{\partial k_x} = \begin{bmatrix}\frac{1}{mi}\frac{\partial}{\partial x} & i\lambda\theta(-x) & 0 & 0\\ -i\lambda\theta(-x) & \frac{1}{mi}\frac{\partial}{\partial x} & 0 & 0\\ 0 & 0 & -\frac{1}{mi}\frac{\partial}{\partial x} & -i\lambda\theta(-x)\\ 0 & 0 & i\lambda\theta(-x) & -\frac{1}{mi}\frac{\partial}{\partial x}\end{bmatrix}. \tag{27}$$

By solving Eq. (26), we determine a_1 and b_1 and obtain the normalized tunneling conductance [22],

$$\sigma(eV) = \frac{\int_{-\theta_C}^{\theta_C} \sigma_S(eV,\theta_S)d\theta_S}{\int_{-\theta_C}^{\theta_C} \sigma_N(eV,\theta_S)d\theta_S}, \tag{28}$$

$$\sigma_S(eV,\theta_S) = 4e(1+|a_1|^2-|r_1|^2)\left(\frac{k_1\cos\theta_N}{m}(|s|^2+1) - i\lambda(s-s^*)\right). \tag{29}$$

σ_S (σ_N) represents the tunneling conductance in the ARM/S junction [the ARM/normal metal ($\Delta_0 = 0$) junction]. In Sec. III, we also show the tunneling conductance of the one-dimensional limit by choosing $k_y = 0$.

III. RESULTS AND DISCUSSIONS

In this and the next sections, we show and discuss the obtained tunneling conductance of ARM/S junctions for various types of pairing symmetry, where dimensionless parameters $\alpha = \frac{m\lambda^2}{\mu_S}$, $\gamma = \frac{\mu_N}{\mu_S}$, $h = \frac{H}{\mu_S}$, and $Z = \frac{V_0 k_S}{\mu_S}$ are used. For simplicity, in the following sections we use abbreviations for superconducting junctions, e.g., ARM/s-waves and ARM/spin-singlets.

A. ARM/s-wave superconductor junction

In this subsection, we discuss two-dimensional ARM/s-wave superconductor junctions with

$$f_{\theta_S} = 1. \tag{30}$$

We calculate the normalized tunneling conductance $\sigma(eV)$ in Eq. (28) using the formulation in Sec. II. First, we show the obtained conductance without an insulating barrier, i.e., $Z = 0$, as a function of bias voltage. Figure 5 shows the $\sigma(eV)$ of an N/s-wave (a), FM/s-waves (b), and ARM/s-waves (c) for $\gamma = 1$. In Fig. 5(a), we find $\sigma(|eV| < \Delta_0) = 2$ by the perfect Andreev reflection at the interface [46,47]. As shown in Fig. 5(b), in FM/S junctions, the $\sigma(eV)$ are shown for various magnitudes of the exchange field, namely h. The magnitude of the inner gap conductance $\sigma(|eV| < \Delta_0)$ is suppressed with the increase in h. In particular, the $\sigma(|eV| < \Delta_0)$ becomes zero for $h > 1$, where the ferromagnet is fully polarized [see Fig. 5(b)(iii)]. As shown in Fig. 5(c), the $\sigma(eV)$ for $h > 1$ is enhanced with the increase in the magnitude of the RSOI α. The qualitative features of the $\sigma(eV)$ in Fig. 5(c) can be interpreted by the spin configuration of the ARM.

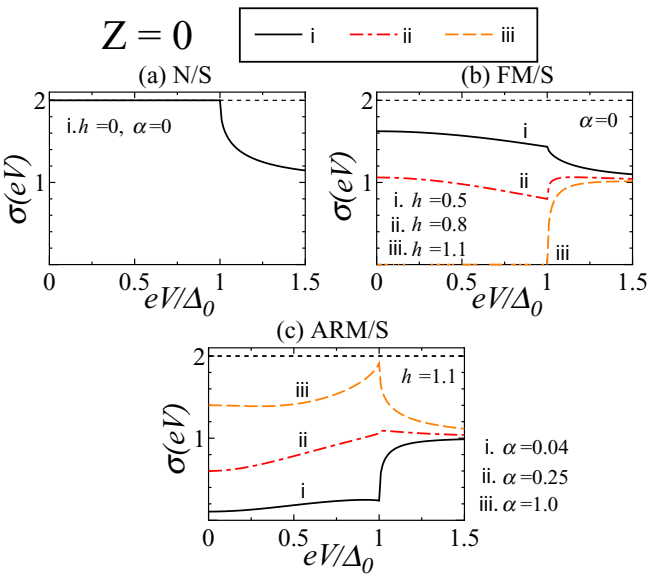

FIG. 5. (Color online) Normalized tunneling conductance $\sigma(eV)$ of two-dimensional (a) N/S, (b) FM/S, and (c) ARM/S junctions without an insulating barrier ($Z = 0$), where S is chosen as the s-wave superconductor. We use $\gamma = 1.0$ in all cases.

To see this, we calculate the spin configuration in the ARM. Using the eigenfunction of the ARM, $\psi(\boldsymbol{k}_1) = (\frac{s_{\boldsymbol{k}_1}}{\sqrt{|s_{\boldsymbol{k}_1}|^2+1}}, \frac{1}{\sqrt{|s_{\boldsymbol{k}_1}|^2+1}})^T$, the spin direction of electron and hole states is defined by $\langle \boldsymbol{S}_e(\boldsymbol{k}_1)\rangle \equiv \langle\psi(\boldsymbol{k}_1)|\hat{\boldsymbol{\sigma}}|\psi(\boldsymbol{k}_1)\rangle$ and $\langle \boldsymbol{S}_h(\boldsymbol{k}_1)\rangle \equiv \langle\psi(-\boldsymbol{k}_1)^*|\hat{\boldsymbol{\sigma}}^*|\psi(-\boldsymbol{k}_1)^*\rangle$, respectively. In the above, $s_{\boldsymbol{k}_1}$ is given by $s_{\boldsymbol{k}_1} = -\frac{\lambda(ik_{1x}+k_{1y})}{\xi_{\boldsymbol{k}_1}+H}$, where $k_{1x(y)}$ is an x (y) component of $\boldsymbol{k}_1$. The explicit forms of $\langle \boldsymbol{S}_e(\boldsymbol{k}_1)\rangle$ and $\langle \boldsymbol{S}_h(\boldsymbol{k}_1)\rangle$ become

$$\begin{aligned}\langle \boldsymbol{S}_e(\boldsymbol{k}_1)\rangle &= (\langle S_{xe}(\boldsymbol{k}_1)\rangle, \langle S_{ye}(\boldsymbol{k}_1)\rangle, \langle S_{ze}(\boldsymbol{k}_1)\rangle)\\ &= \left(\frac{-2\lambda k_{1y}\epsilon_{\boldsymbol{k}_1}}{(\lambda k_1)^2+\epsilon_{\boldsymbol{k}_1}^2}, \frac{2\lambda k_{1x}\epsilon_{\boldsymbol{k}_1}}{(\lambda k_1)^2+\epsilon_{\boldsymbol{k}_1}^2}, \frac{(\lambda k_1)^2-\epsilon_{\boldsymbol{k}_1}^2}{(\lambda k_1)^2+\epsilon_{\boldsymbol{k}_1}^2}\right),\end{aligned} \tag{31}$$

$$\begin{aligned}\langle \boldsymbol{S}_h(\boldsymbol{k}_1)\rangle &= (\langle S_{xh}(\boldsymbol{k}_1)\rangle, \langle S_{yh}(\boldsymbol{k}_1)\rangle, \langle S_{zh}(\boldsymbol{k}_1)\rangle)\\ &= \left(\frac{2\lambda k_{1y}\epsilon_{-\boldsymbol{k}_1}}{(\lambda k_1)^2+\epsilon_{-\boldsymbol{k}_1}^2}, \frac{-2\lambda k_{1x}\epsilon_{-\boldsymbol{k}_1}}{(\lambda k_1)^2+\epsilon_{-\boldsymbol{k}_1}^2}, \frac{(\lambda k_1)^2-\epsilon_{-\boldsymbol{k}_1}^2}{(\lambda k_1)^2+\epsilon_{-\boldsymbol{k}_1}^2}\right),\end{aligned} \tag{32}$$

with

$$\epsilon_{\boldsymbol{k}_1} = \xi_{\boldsymbol{k}_1} + H. \tag{33}$$

If we choose $\lambda = 0$, we can reproduce the FPFM case. From Eqs. (4), (31), and (32), while the signs of the in-plane components of each spin expectation value are opposite, the z component is the same:

$$\begin{aligned}\langle S_{ze}(\boldsymbol{k}_1)\rangle &= \langle S_{zh}(\boldsymbol{k}_1)\rangle\\ &= -\frac{1}{1+\frac{2\alpha}{h}+\frac{2\alpha(1-h)}{h(h+\alpha+\sqrt{\alpha^2+2\alpha+h^2})}}.\end{aligned} \tag{34}$$

For Eq. (34), we can find that, if $\alpha \gg h$, $\langle S_{ze}(\boldsymbol{k}_1)\rangle$ and $\langle S_{zh}(\boldsymbol{k}_1)\rangle$ approach zero [see Fig. 6(a)]. On the other hand, the magnitudes of $\langle S_{x(y)e}(\boldsymbol{k}_1)\rangle$ and $\langle S_{x(y)h}(\boldsymbol{k}_1)\rangle$ become larger as the magnitude of the RSOI increases. These indicate that the spin in the ARM is not fully polarized along the z axis and its direction has an xy-plane component unlike the FPFM. We

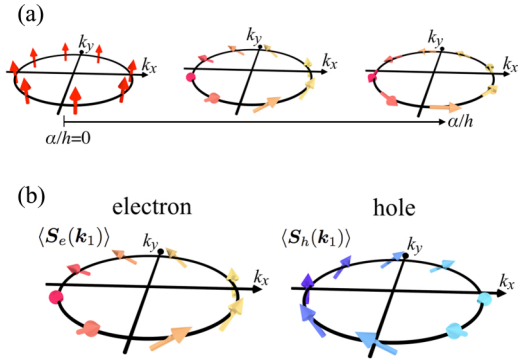

FIG. 6. (Color online) Schematic illustration of the spin configuration in the ARM. (a) The α/h dependence of the spin configuration and (b) the spin configuration of an electron and hole is shown.

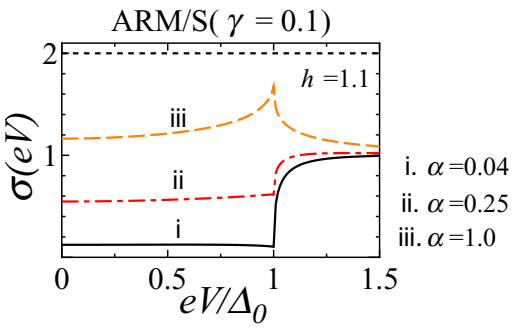

FIG. 8. (Color online) Normalized tunneling conductance $\sigma(eV)$ of two-dimensional ARM/S junctions without an insulating barrier ($Z = 0$), where S is chosen as the s-wave superconductor. We use $\gamma = 0.1$ in all cases.

show later that the x and y components of the spin polarization induced by the RSOI do not suppress the magnitude of the $\sigma(|eV| < \Delta_0)$ in the ARM/spin-singlet. As a preparation for showing it, we explain why the tunneling conductance in FPFM/spin-singlets is reduced by the exchange field. Figure 7 shows the scattering process in which an electron with down-spin is injected from the left side. In this case, the spin of an incident electron is flipped through the Andreev reflection because we assume the spin-singlet superconductor for $x > 0$. However, the Andreev reflection for $|eV| < \Delta_0$ does not occur in the FPFM/spin-singlets since there is no corresponding Fermi surface for the hole state with up-spin. Equations (31) and (32) confirm this since $\langle S_{ze}(\boldsymbol{k}_1)\rangle = \langle S_{zh}(\boldsymbol{k}_1)\rangle = -1$ is satisfied in the FPFM. This is because the Andreev reflection is suppressed in FPFM/spin-singlets. In addition, the suppression of the Andreev reflection reduces the inner gap conductance, as we can see from

$$\sigma(eV) \propto 1 - |r|^2 + |a|^2, \tag{35}$$

where r (a) is a normal (Andreev) reflection coefficient. Therefore, the tunneling conductance decreases because of the exchange field in FPFM/spin-singlets. On the other hand, for $\lambda \neq 0$, $\langle S_{x(y)e}(\boldsymbol{k}_1)\rangle$ and $\langle S_{x(y)h}(\boldsymbol{k}_1)\rangle$ become nonzero and satisfy

$$\langle S_{xe}(\boldsymbol{k}_1)\rangle = -\langle S_{xh}(\boldsymbol{k}_1)\rangle, \tag{36}$$
$$\langle S_{ye}(\boldsymbol{k}_1)\rangle = -\langle S_{yh}(\boldsymbol{k}_1)\rangle \tag{37}$$

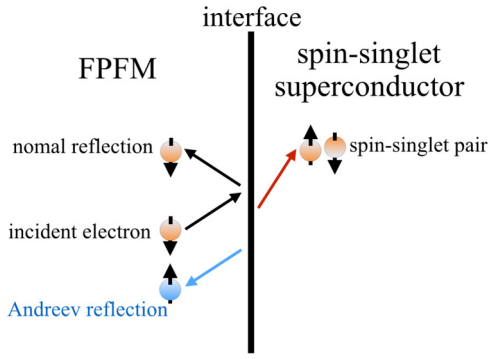

FIG. 7. (Color online) Schematic illustration of the scattering process at the interface of FPFM/spin-singlet superconductor junctions.

in the ARM, as shown in Fig. 6(b). This means that the coefficient of the Andreev reflection recovers due to the RSOI in the ARM/spin-singlets by comparison with the FPFM/spin-singlets. Accordingly, the presence of the RSOI enhances the magnitude of the inner gap conductance in ARM/spin-singlets. The above explanation is consistent with the results in Fig. 5(c).

Also, we calculate the $\sigma(eV)$ of ARM/s-waves with $\gamma = 0.1$ because $\gamma < 1$ should be satisfied in realistic cases. The results are shown in Fig. 8. Since the $\sigma(|eV| < \Delta_0)$ in Fig. 8 is enhanced with the increase in α, it is found that the change of γ does not qualitatively influence the feature of the $\sigma(eV)$ in ARM/s-waves. In addition, even for junctions with an anisotropic superconductor, the qualitative features of $\sigma(eV)$ are insensitive to the change of γ. Therefore, we mainly focus on $\gamma = 1$ below.

Next, tunneling conductance in the one-dimensional limit, which corresponds to angle-resolved conductance with perpendicular injection ($k_y = 0$), is studied. Figure 9 shows $\sigma(eV)$ of the one-dimensional system for $Z = 0$. The indices of Figs. 9(a)–9(c) correspond with those of Fig. 5. As we can see from Figs. 9(a) and 9(b), for an N/s-wave and FM/s-waves, the qualitative behaviors of $\sigma(eV)$ in the one-dimensional limit are similar to those in two-dimensional cases [46,47]. Figure 9(c) also indicates that the $\sigma(|eV| < \Delta_0)$ increases due to the RSOI [see Fig. 9(b)(iii)]. However, note that zero-bias conductance (ZBC), i.e., $\sigma(eV = 0)$, is zero regardless of the change of α. This is because, in the one-dimensional cases, $|a_1|^2 = 0$ and $|r_1|^2 = 1$ are satisfied for $eV = 0$ in Eq. (29). This profile of $\sigma(eV = 0)$ does not correspond with that in the corresponding two-dimensional cases, but the result is consistent with previous studies [48–50]. According to one of the previous studies [49], in which the conductance was calculated using the scattering matrix theory, the ZBC should be quantized to be 0 or 2 if half of the spin degrees of freedom and the one-channel system are realized in the normal metallic region. Moreover, if the superconductor in the junction is topologically trivial, ZBC should be zero [49]. In our model, the one-dimensional ARM is just a one-channel system, and we consider the topologically trivial s-wave superconductor in $x > 0$. Hence, the ZBC should be zero in the one-dimensional ARM/s-waves.

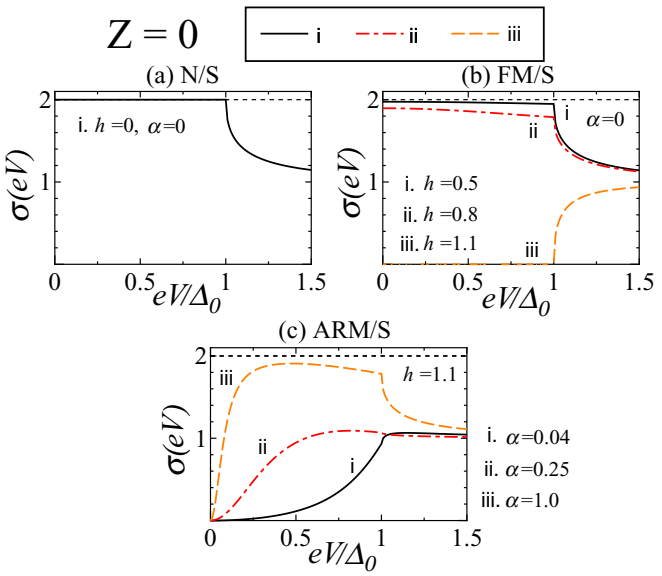

FIG. 9. (Color online) Normalized $\sigma(eV)$ of (a) N/S, (b) FM/S, and (c) ARM/S junctions without an insulating barrier ($Z = 0$) in the one-dimensional limit, where S is chosen as the s-wave superconductor. We use $\gamma = 1.0$ in all cases.

Then, we show tunneling conductance with a high-barrier case ($Z = 10$) for two-dimensional junctions. $\sigma(eV)$ of an N/s-wave, FM/s-waves, and ARM/s-waves are plotted in Figs. 10(a)–10(c), respectively. In these cases, all of the line shapes of $\sigma(eV)$ show conventional U-shaped structures regardless of the change of α and h (see Fig. 10) since the $\sigma(|eV| < \Delta_0)$ is strongly reduced by the insulating barrier due to the absence of the SABS. In other words, the coexistence of the exchange field and the RSOI does not qualitatively affect $\sigma(eV)$ for the high-barrier case.

B. ARM/d-wave superconductor junction

To understand the effect of an SABS [3,5] on the charge transport of ARM/S junctions, we calculate the tunneling conductance in two-dimensional ARM/d-wave superconductor junctions in this subsection. As a typical example of a d-wave superconductor, we choose $d_{x^2-y^2}$-wave and d_{xy}-wave pair potentials. In these cases, f_{θ_S} is given by

$$f_{\theta_S} = \begin{cases} \cos(2\theta_S) & (d_{x^2-y^2}\text{-wave}), \\ \sin(2\theta_S) & (d_{xy}\text{-wave}). \end{cases} \tag{38}$$

First, using f_{θ_S}, tunneling conductance for $Z = 0$ is studied. It is known that, in FM/d-waves, the inner gap conductance is suppressed by the exchange field, and the ZBC becomes zero when the ferromagnet is fully polarized. As we have discussed in Sec. III A, in ARM/spin-singlets, the inner gap conductance is recovered upon increasing the magnitude of the RSOI. ARM/d-waves also show an enhancement of the inner gap conductance due to the RSOI. In addition, the qualitative features of the tunneling conductance do not depend on whether the paring symmetry is $d_{x^2-y^2}$-wave or d_{xy}-wave.

Next, we focus on the tunneling conductance for the high-barrier case ($Z = 10$). The line shape of $\sigma(eV)$ becomes the conventional V-shaped structure for $d_{x^2-y^2}$-wave superconductor junctions regardless of the change of α and h. This is because the $\sigma(eV)$ is strongly reduced by the insulating barrier.

In contrast, $\sigma(eV)$ shows a drastic feature due to the presence of an SABS in ARM/d_{xy}-waves. It is known that the $\sigma(eV)$ in N/d_{xy}-waves have a ZBCP, which is enhanced upon increasing Z [see Fig. 11(a)] [5]. On the other hand, when we consider FM/d_{xy}-waves, the height of the ZBCP becomes lowered with an increase in h, as shown in Fig. 11(b)

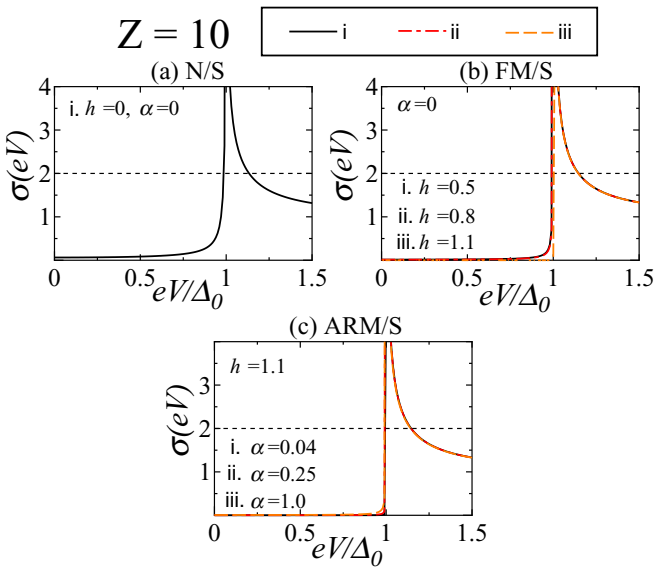

FIG. 10. (Color online) Normalized $\sigma(eV)$ of two-dimensional (a) N/S, (b) FM/S, and (c) ARM/S junctions with a high tunneling barrier ($Z = 10$), where S is chosen as an s-wave superconductor. We use $\gamma = 1.0$ in all cases.

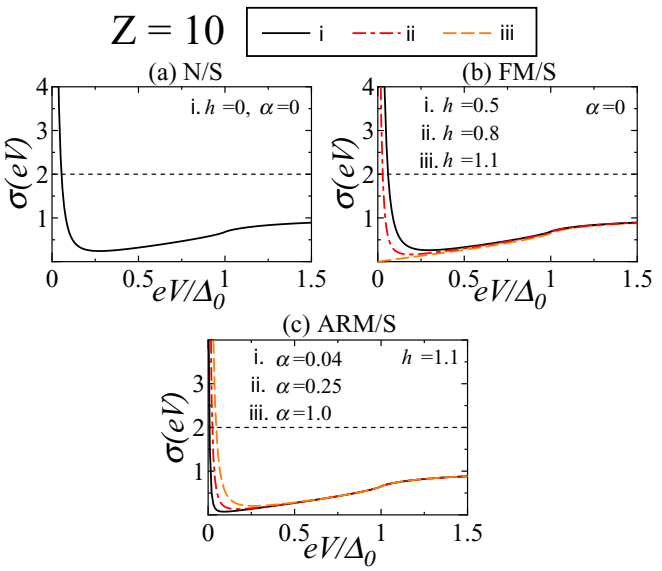

FIG. 11. (Color online) Normalized $\sigma(eV)$ of two-dimensional (a) N/S, (b) FM/S, and (c) ARM/S junctions with a high tunneling barrier ($Z = 10$), where S is chosen as the d_{xy}-wave superconductor. We use $\gamma = 1.0$ in all cases.

[13,14,16]. In particular, when the ferromagnet is fully polarized, the ZBCP completely disappears [13,14,16,17] [see Fig. 11(b)(iii)]. We find that, in ARM/d_{xy}-waves, the ZBCP appears again due to the presence of α [see Fig. 11(c)]. Moreover, the height of the ZBCP becomes larger as α increases. This α dependence of $\sigma(eV=0)$ can be understood by the spin configuration of the ARM, which is discussed in the s-wave superconductor junction (see Sec. III A). As the magnitude of the RSOI increases, the z component of spin polarization by the exchange field decreases. Additionally, the spin polarization by the RSOI does not suppress the tunneling conductance of ARM/spin-singlets, as mentioned in Sec. III A. This implies that the ZBCP can remain in ARM/d_{xy}-waves by the RSOI as compared to FPFM/d_{xy}-waves [see Figs. 11(b) and 11(c)].

Based on the results in Fig. 11(c), we discuss the physical origin of the presence of ZBCP in an FM/d_{xy}-wave with the insulating barrier from the aspect of an experiment on $La_{0.67}Sr_{0.33}MnO_3$ (LSMO)/$YBa_2Cu_3O_{7-\delta}$ (YBCO) with a (110) oriented thin-film junction [51]. In the experiment, the dependence of $\sigma(eV)$ on the magnitude of the magnetic field applied along the in-plane direction has been shown. Surprisingly, the ZBCP remains despite the strongly applied magnetic field, where LSMO is known as a half-metallic material where spin is fully polarized. Specifically, the experimental setup [51] does not exactly correspond with our model. In the experiment, the exchange field points toward the xy-plane direction, while it is parallel to the z axis in our model. However, also in the junction of the experiment, RSOI $\lambda(\hat{\boldsymbol{\sigma}}\times\boldsymbol{k})\cdot\boldsymbol{i}$ can exist near the interface due to the breakdown of inversion symmetry. Here, $\boldsymbol{i}$ is a unit vector perpendicular to the interface, i.e., $\boldsymbol{i}||\boldsymbol{x}$. Since this RSOI $\lambda(\hat{\boldsymbol{\sigma}}\times\boldsymbol{k})\cdot\boldsymbol{x}$ induces the z component of the spin polarization and decreases the xy-plane component of the spin polarization induced by the magnetic field and the magnetization, LSMO near the interface can behave like the ARM. Accordingly, in light of our theory, the ZBCP in the FPFM/d_{xy}-wave is allowed in the presence of the RSOI. Therefore, the conductance of Kashiwaya's experiment [51] may be interpreted from the viewpoint of ARM/d_{xy}-waves. To compare the experiment and theoretical predictions in detail, it is necessary to take into account the surface roughness effect.

C. ARM/spin-triplet p-wave superconductor junctions

In this subsection, we study ARM/spin-triplet p-wave superconductor junctions. We focus mainly on the tunneling conductance for ARM/p_x-waves and ARM/p_y-waves for several directions of the $\boldsymbol{d}$ vector. To understand the influence of the RSOI on the tunneling conductance, we compare the results of ARM/p_x-waves with ARM/p_y-waves. g_{θ_S} in Eq. (13) is given as follows: for the p_x-wave and p_y-wave symmetries,

$$g_{\theta_S}=\begin{cases}\cos(\theta_S) & (p_x\text{-wave}),\\ \sin(\theta_S) & (p_y\text{-wave}).\end{cases} \tag{39}$$

First, Fig. 12 shows the tunneling conductance of two-dimensional junctions with a p_x-wave superconductor for $Z=0$. Figures 12(A), 12(B), and 12(C) correspond to the cases with $\boldsymbol{d}||\boldsymbol{x}$, $\boldsymbol{d}||\boldsymbol{y}$, and $\boldsymbol{d}||\boldsymbol{z}$, respectively. The indices (a), (b), and (c) denote N/p_x-waves, FM/p_x-waves, and

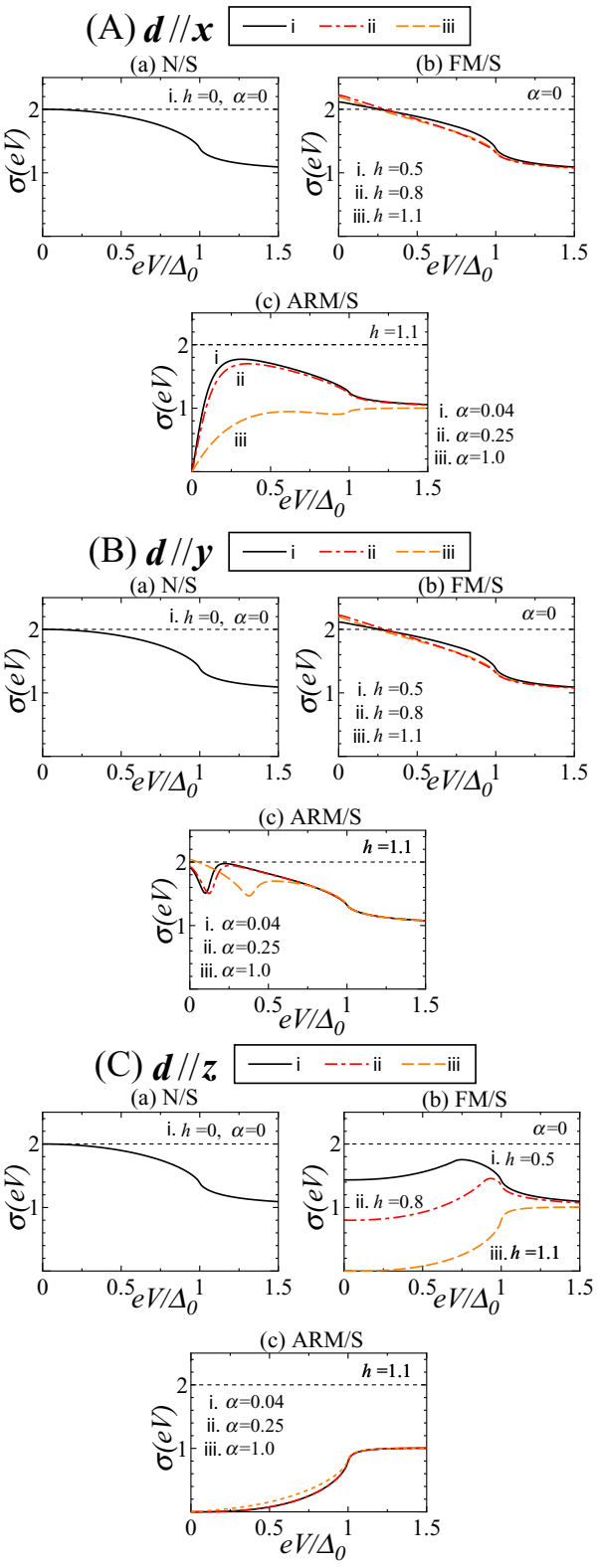

FIG. 12. (Color online) Normalized $\sigma(eV)$ of two-dimensional (a) N/S, (b) FM/S, and (c) ARM/S junctions without insulating barrier ($Z=0$), where S is chosen as the p_x-wave superconductor for (A) $\boldsymbol{d}\parallel\boldsymbol{x}$, (B) $\boldsymbol{d}\parallel\boldsymbol{y}$, and (C) $\boldsymbol{d}\parallel\boldsymbol{z}$. We use $\gamma=1$ in all cases.

ARM/p_x-waves, respectively. For the N/p_x-waves, we have $\sigma(eV=0)=2$ independent of the direction of the $\boldsymbol{d}$ vector due to the perfect Andreev reflection in $Z=0$ [47] [see

Figs. 12(A)(a), 12(B)(a), and 12(C)(a)]. On the other hand, the ZBC changes from $\sigma(eV=0)=2$ in FM/p_x-waves. The change of the $\sigma(eV=0)$ depends on the direction of the $\boldsymbol{d}$ vector as well as the magnitude of the exchange field h. When the $\boldsymbol{d}$ vector is perpendicular to the exchange field, the $\sigma(eV=0)$ changes slightly [see Figs. 12(A)(b) and 12(B)(b)]. However, when the $\boldsymbol{d}$ vector is parallel to the exchange field, the $\sigma(eV=0)$ is significantly reduced with the magnitude of h [see Fig. 12(C)(b)]. Now, let us show $\sigma(eV)$ in ARM/p_x-waves. We find that $\sigma(eV=0)$ is zero for $\boldsymbol{d}||\boldsymbol{x}$ and $\boldsymbol{d}||\boldsymbol{z}$, but $\sigma(eV=0)$ is nonzero only for $\boldsymbol{d}||\boldsymbol{y}$. As we can see from Figs. 12(A)(c) and 12(C)(c), the inner gap conductance for $\boldsymbol{d}||\boldsymbol{z}$ is insensitive to the magnitude of the RSOI, while that for $\boldsymbol{d}||\boldsymbol{x}$ changes with the magnitude of the RSOI. In addition, the $\sigma(eV=0)$ does not depend strongly on the magnitude of the RSOI, and $\sigma(eV=0)\sim 2$ is satisfied for $\boldsymbol{d}||\boldsymbol{y}$ [see Fig. 12(B)(c)]. As we will show later, the dependence of $\sigma(eV)$ of ARM/p_x-waves on the direction of the $\boldsymbol{d}$ vector can be explained by a winding number, which is a topological invariant ensuring the presence of a zero-energy SABS.

To explain the above anomalous property of $\sigma(eV)$ in ARM/p_x-waves, we show the tunneling conductance in two-dimensional ARM/p_y-waves for $Z=0$. Comparing the results in ARM/p_y-waves with those in ARM/p_x-waves is important because the SABS is absent in junctions with a p_y-wave superconductor, unlike those with a p_x-wave superconductor [52]. Figure 13 shows $\sigma(eV)$ of the junctions with a p_y-wave superconductor. The indices of Figs. 13(A), 13(B), and 13(C) [(a), (b), and (c)] are the same as those of Fig. 12, respectively. As we can see from Figs. 13(A)(a), 13(A)(b), 13(B)(a), 13(B)(b), 13(C)(a), and 13(C)(b) [9,19], the behaviors of the inner gap conductance $\sigma(|eV|<\Delta_0)$ in N/p_y-waves and FM/p_y-waves are qualitatively similar to those in the junctions with a p_x-wave superconductor. However, the behaviors of $\sigma(eV=0)$ of the ARM/p_y-waves are qualitatively different from those of the ARM/p_x-waves. In the ARM/p_y-waves, regardless of the direction of the $\boldsymbol{d}$ vector, the $\sigma(eV=0)$ is not zero despite finite α. To be specific, the $\sigma(eV=0)$ recovers as α increases for $\boldsymbol{d}||\boldsymbol{z}$ [see Fig. 13(C)(c)], while that for $\boldsymbol{d}||\boldsymbol{x}$ and $\boldsymbol{d}||\boldsymbol{y}$ is slightly reduced [see Figs. 13(A)(c) and 13(B)(c)]. As we describe below, these behaviors of the $\sigma(eV=0)$ of ARM/p_y-waves can be understood by the spin configuration of the ARM. In spin-triplet superconductor junctions for $\boldsymbol{d}||\boldsymbol{z}$, when an electron with up-spin injects, the Andreev-reflected hole has down-spin similar to the spin-singlet superconductor junction cases. This indicates that the $\sigma(|eV|<\Delta_0)$ for $\boldsymbol{d}||\boldsymbol{z}$ is suppressed by the exchange field and is enhanced by the RSOI, as shown in Figs. 13(C)(b) and 13(C)(c). On the other hand, when an electron with up-spin injects, the Andreev reflection must occur with an up-spin hole for $\boldsymbol{d}||\boldsymbol{x}$ and $\boldsymbol{d}||\boldsymbol{y}$. Hence, the $\sigma(eV)$ is not reduced in the junctions with the FPFM for $\boldsymbol{d}||\boldsymbol{x}$ and $\boldsymbol{d}||\boldsymbol{y}$ [see Figs. 13(A)(b)(iii) and 13(B)(b)(iii)]. However, in the ARM, the RSOI reduces the z component of the spin polarization, as we discussed in Sec. III A. Accordingly, the $\sigma(|eV|<\Delta_0)$ decreases in the ARM/p_y-waves with $\boldsymbol{d}||\boldsymbol{x}$ and $\boldsymbol{d}||\boldsymbol{y}$, contrary to those with $\boldsymbol{d}||\boldsymbol{z}$. Therefore, the discussion about the spin configuration supports our calculations.

Now, we discuss the results of ARM/p_x-waves. In ARM/p_x-waves, the dependence of $\sigma(eV=0)$ on the direction of the $\boldsymbol{d}$ vector is qualitatively different from that in ARM/p_y-waves. In addition, as we mentioned above, one of the important differences between the superconducting tunnel

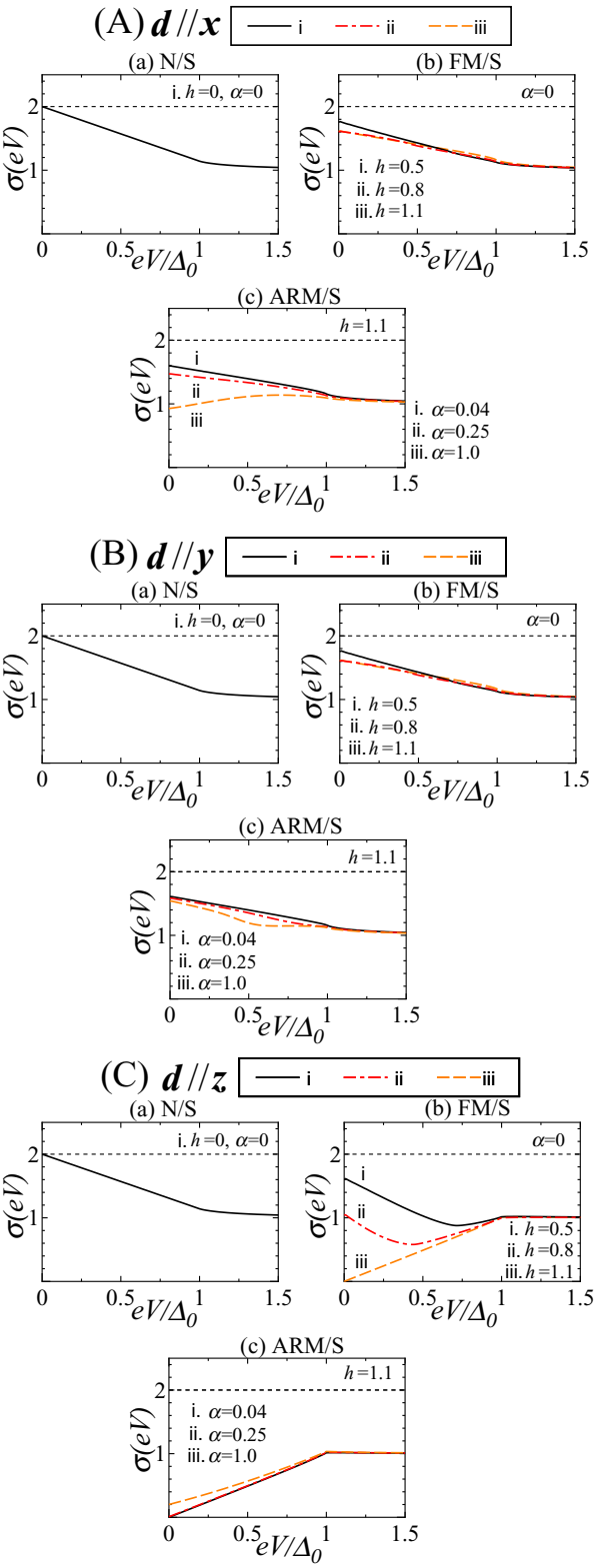

FIG. 13. (Color online) Normalized $\sigma(eV)$ of two-dimensional (a) N/S, (b) FM/S, and (c) ARM/S junctions without an insulating barrier ($Z=0$), where SC is chosen as the p_y-wave superconductor for (A) $\boldsymbol{d}\parallel\boldsymbol{x}$, (B) $\boldsymbol{d}\parallel\boldsymbol{y}$, and (C) $\boldsymbol{d}\parallel\boldsymbol{z}$. We use $\gamma=1$ in all cases.

junctions with the p_x-wave superconductor and those with the p_y-wave superconductor is whether the SABS can exist or not. To understand the behavior of $\sigma(eV=0)$ in ARM/p_x-waves, we introduce a winding number W for the one-dimensional limit ($k_y=0$). Here, W takes an integer and is defined by a chiral operator $\bar{\Gamma}$ [52,53] and a BdG Hamiltonian $\bar{H}$,

$$W \equiv \frac{-1}{4\pi i}\int dk_x[\bar{\Gamma}\bar{H}^{-1}(\boldsymbol{k})\partial_{k_x}\bar{H}(\boldsymbol{k})], \tag{40}$$

where the chiral operator anticommutes with the BdG Hamiltonian, and the line integral in Eq. (40) should be performed in the first Brillouin zone. When the winding number W is nonzero, the SABS exists at the surface of the superconductor. For a spin-triplet superconductor, a chiral operator generally depends on the direction of the $\boldsymbol{d}$ vector (see Appendix A). In particular, for the p_x-wave superconductor, the chiral operator leading to a nontrivial W is given by

$$\bar{\Gamma} = \begin{cases} \hat{\sigma}_z\hat{\tau}_y & (\boldsymbol{d}||\boldsymbol{x}), \\ \hat{\sigma}_0\hat{\tau}_x & (\boldsymbol{d}||\boldsymbol{y}), \\ -\hat{\sigma}_x\hat{\tau}_y & (\boldsymbol{d}||z), \end{cases} \tag{41}$$

and the resulting W satisfies $W=2$. In the ARM/p_x-waves, the SABS is influenced by the RSOI and the exchange field through electrons and holes in the ARM. From Eq. (41), we find that the chiral operator anticommutes with the terms of the RSOI $\lambda k_x\hat{\sigma}_y\hat{\tau}_z$ and the exchange field $H\hat{\sigma}_z\hat{\tau}_z$ only for $\boldsymbol{d}||\boldsymbol{y}$. This indicates that the chiral symmetry protecting the SABS survives under the RSOI and the exchange field only when $\boldsymbol{d}||\boldsymbol{y}$. Therefore, we can understand the RSOI dependence of the tunneling conductance in the ARM/p_x-waves from a topological point of view. The discussion about W and the symmetries are given in Appendix A.

Below, using the numerical results, we check the validity of the above discussion on W. As written in Appendix A, the RSOI breaks the symmetry protecting the SABS for $\boldsymbol{d}||\boldsymbol{x}$ and $\boldsymbol{d}||z$. This means that the resulting W is nonzero only for $\boldsymbol{d}||\boldsymbol{y}$ even if the exchange field does not exist. Accordingly, the property of the tunneling conductance in ARM/p_x-waves can be realized in the junctions with a nonmagnetic metal where the RSOI exists, which we call a Rashba metal (RM). To check whether the property of the tunneling conductance of the ARM/p_x-waves and that of the RM/p_x-waves are similar to each other, we calculate the tunneling conductance of the RM/p_x-waves. In Fig. 14, the normalized tunneling conductance $\sigma_1(eV)$, where an electron of the outer Fermi surface of RM injects [28], is shown for several directions of the $\boldsymbol{d}$ vector. The details of the formulation are written in Appendix B. It is found that $\sigma_1(eV)$ is suppressed as the inner Fermi surface becomes smaller for $\boldsymbol{d}||\boldsymbol{x}$ and $\boldsymbol{d}||z$ [see Figs. 14(a) and 14(c)]. In particular, for $\boldsymbol{d}||\boldsymbol{x}$ and $\boldsymbol{d}||z$, the $\sigma_1(eV=0)$ is completely reduced for $\mu_N\to 0$, where the inner Fermi surface of the RM disappears like that of the ARM. In contrast, $\sigma_1(eV=0)$ is insensitive to γ for $\boldsymbol{d}||\boldsymbol{y}$. From these results, it is found that the RSOI dominantly contributes to the anomalous property of the tunneling conductance in the ARM/p_x-waves while the exchange field does not contribute as much. This is consistent with the discussion with the winding number. Next, we also calculate how the direction of the $\boldsymbol{d}$ vector influences $\sigma(eV=0)$ in ARM/p_x-waves, as shown in Fig. 15. A sharp peak appears for $\boldsymbol{d}||\boldsymbol{y}$ in the one-dimensional limit, although a broad peak appears in the two-dimensional

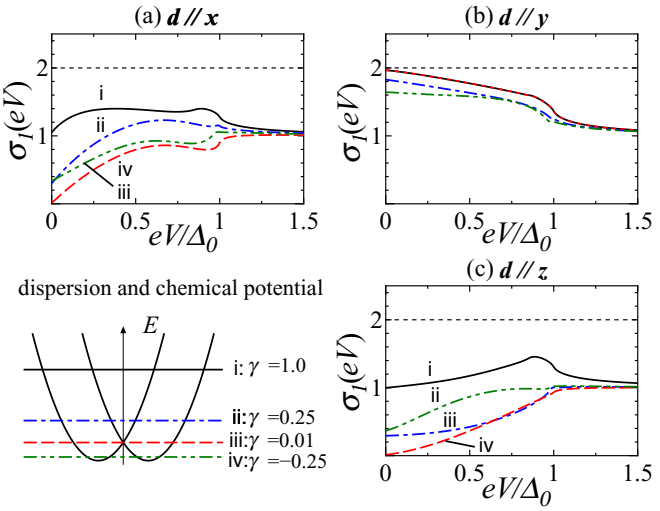

FIG. 14. (Color online) Normalized tunneling conductance $\sigma_1(eV)$ of two-dimensional RM/p_x-wave superconductor junctions for $Z=0$ for various chemical potentials μ_N. $\sigma_1(eV)$ is shown for (a) $\boldsymbol{d}||\boldsymbol{x}$, (b) $\boldsymbol{d}||\boldsymbol{y}$, and (c) $\boldsymbol{d}||z$. We use $\alpha=1$ and $h=0$.

system. The sharp peak in the one-dimensional limit is consistent with our discussion based on the winding number.

Finally, $\sigma(eV)$ in ARM/p_x-waves for the high barrier case ($Z=10$) is studied. Figure 16 shows the obtained $\sigma(eV)$ of N/p_x-waves (a), FM/p_x-waves (b), and ARM/p_x-waves (c) for $\boldsymbol{d}||\boldsymbol{y}$. In the N/$p_x$-waves, a ZBCP appears [see Fig. 16(a)] due to the existence of the SABS regardless of the direction of the $\boldsymbol{d}$ vector [4,5,54,55]. As we have mentioned already, the inner gap conductance does not decrease in FM/spin-triplets when the $\boldsymbol{d}$ vector is perpendicular to the exchange field [18,19]. For this reason, the ZBCP exists for $\boldsymbol{d}||\boldsymbol{x}$ and $\boldsymbol{d}||\boldsymbol{y}$ [see Fig. 16(b)] while the height of the ZBCP is reduced by the exchange field for $\boldsymbol{d}||z$. In ARM/p_x-waves, the $\sigma(eV=0)$ is zero for $\boldsymbol{d}||\boldsymbol{x}$ and $\boldsymbol{d}||z$ similarly to the cases for $Z=0$, and the ZBCP appears only when $\boldsymbol{d}||\boldsymbol{y}$ [see Fig. 16(c)]. In contrast, the ZBCP does not appear regardless of the change of α and h in superconducting tunnel junctions with a p_y-wave superconductor. This is natural because the SABS does not exist at the surface of a p_y-wave superconductor [4,9].

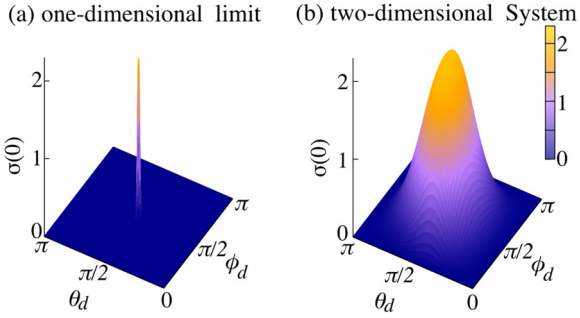

FIG. 15. (Color online) Normalized zero-bias tunneling conductance $\sigma(eV=0)$ of ARM/p_x-wave superconductor junctions for $Z=0$ as functions of the polar angle θ_d and the azimuthal angle ϕ_d of the $\boldsymbol{d}$ vector (see Fig. 4). We use $\gamma=1.0$, $\alpha=1.0$, and $h=1.1$ in both (a) the one-dimensional limit and (b) two-dimensional cases.

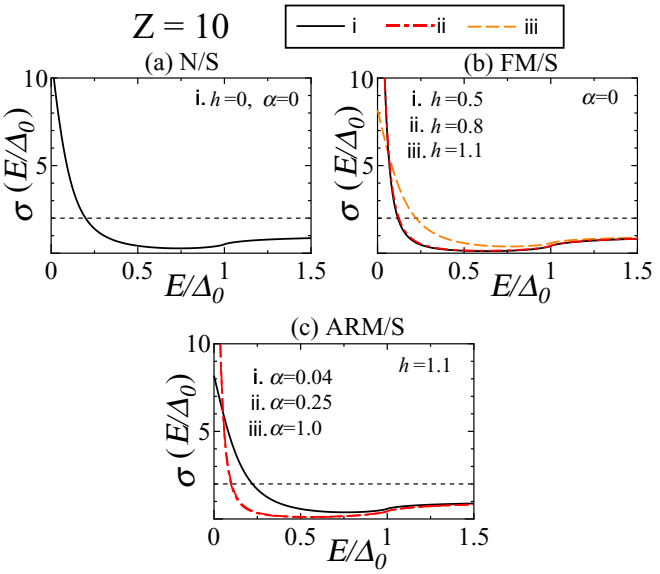

FIG. 16. (Color online) Normalized $\sigma(eV)$ of two-dimensional (a) N/S, (b) FM/S, and (c) ARM/S junctions without an insulating barrier ($Z = 10$), where S is chosen as the p_x-wave superconductor for $\boldsymbol{d}||\boldsymbol{y}$. We use $\gamma = 1.0$ in all cases.

IV. RELEVANCE TO THE PAIRING SYMMETRY IN Sr_2RuO_4

In this section, we study the tunneling conductance $\sigma(eV)$ in ARM/S junctions where a chiral p-wave, a helical p-wave, and a chiral d-wave are chosen as the pairing symmetry in S, respectively. Based on the obtained results, we suggest a new direction to decide the pairing of Sr_2RuO_4. To calculate $\sigma(eV)$ in the systems corresponding to experiments of the tunneling spectroscopy, we focus on the low transparent junctions with $Z = 5$.

It is noted that chiral p-wave pairing is one of the promising candidates of the pairing symmetry in Sr_2RuO_4 [58], where the $\boldsymbol{d}$ vector is along the z axis. g_{θ_S} is given by

$$g_{\theta_S} = \exp(i\theta_S), \tag{42}$$

with $\boldsymbol{d}||z$. First, for an N/chiral p-wave, the resulting conductance has a broad ZBCP reflecting on the linear dispersion of the SABS parallel to the interface, as shown in Fig. 17(A)(a) [7,8,10]. Then, in FM/chiral p-waves, the inner gap conductance $\sigma(|eV| < \Delta_0)$ decreases with the increase in h since we consider the cases for $\boldsymbol{d}||z$ [18,19] [see Fig. 17(A)(b)]. As a limiting case, the inner gap conductance is completely suppressed in an FPFM/chiral p-wave [see Fig. 17(A)(b)(iii)] [17,19]. A comparison with $\sigma(|eV| < \Delta_0)$ in the FPFM/chiral p-wave shows that $\sigma(|eV| < \Delta_0)$ in ARM/chiral p-waves slightly recover in the presence of the RSOI [see Fig. 17(A)(c)].

Next, we look at the helical p-wave case [11], where the pair potential is given by

$$w_{1\theta_S} = \cos(\theta_S), \quad w_{2\theta_S} = \sin(\theta_S). \tag{43}$$

Time-reversal symmetry is not broken in this state. There has been a theoretical proposal that helical p-wave pairing may be possible by tuning the direction of the $\boldsymbol{d}$ vector of Sr_2RuO_4 [59,60]. Then, two branches of SABS are generated

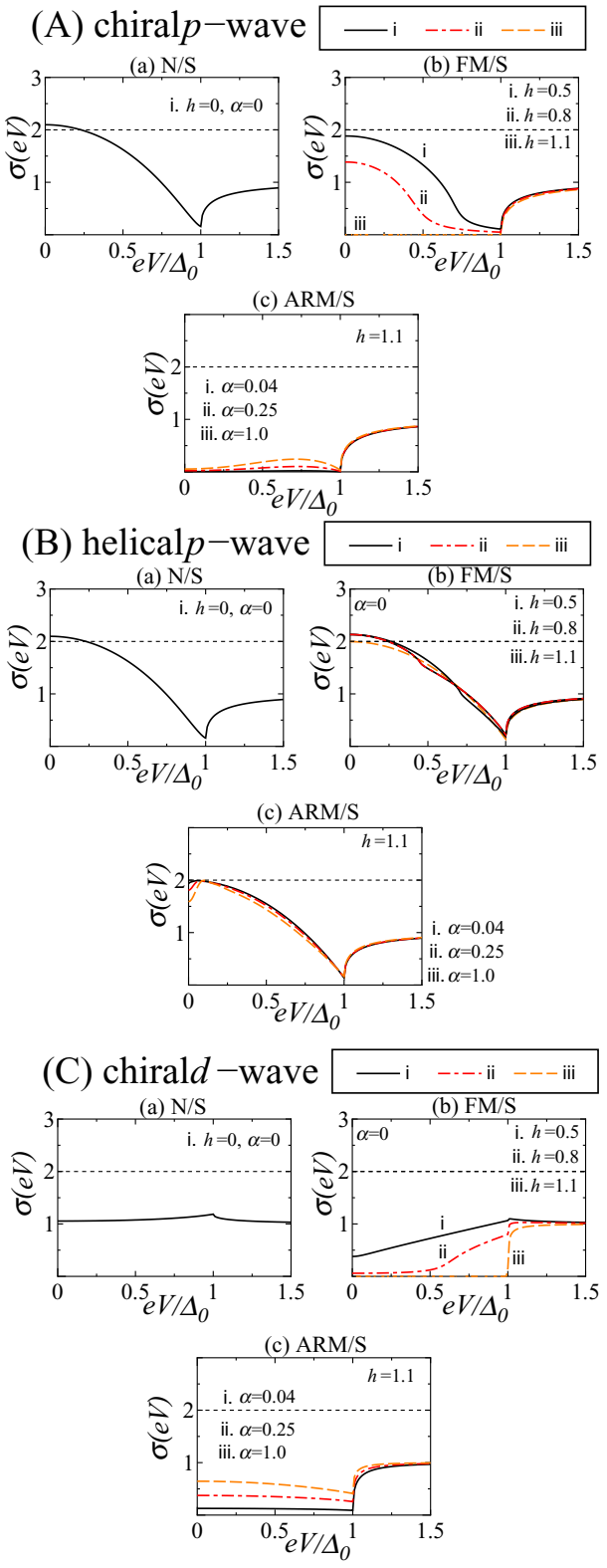

FIG. 17. (Color online) Normalized $\sigma(eV)$ of (a) N/S, (b) FM/S, and (c) ARM/S junctions where S is chosen as the (A) chiral p-wave, (B) helical p-wave, and (C) chiral d-wave superconductors. We use $Z = 5$ and $\gamma = 1.0$ in all cases.

as a Kramers pair. Also in an N/helical p-wave, $\sigma(eV)$ has a broad ZBCP reflecting the linear dispersions of SABS crossing zero energy at $k_y = 0$ similar to that in chiral p-wave

TABLE I. Summary of the behavior of the tunneling conductance $\sigma(eV)$ for the transparent limit and the high barrier case. The first column shows the symmetry of the pair potential in the superconductor. In the first row, X/S and X/I/S indicate the junction for the transparent limit and the high barrier case, respectively. Here, X denotes an N, FM, or ARM.

	$s(d_{x^2-y^2})$-wave	d_{xy}-wave	p_x-wave ($\boldsymbol{d}\|\|\boldsymbol{x}$)	p_x-wave ($\boldsymbol{d}\|\|\boldsymbol{y}$)	p_x-wave ($\boldsymbol{d}\|\|\boldsymbol{z}$)
N/S	$\sigma(0)=2$ [46,47]	$\sigma(0)=2$ [4,5]	$\sigma(0)=2$ [54]	$\sigma(0)=2$ [54]	$\sigma(0)=2$ [8,54,55]
N/I/S	U (V) shape [56]	ZBCP [4,5]	ZBCP [54]	ZBCP [54]	ZBCP [9,54,55]
FM/S	$\sigma(0)\to 0$ for $h\to 1$ [12,57]	$\sigma(0)\to 0$ for $h\to 1$ [13–16]	$\sigma(0)\simeq 2$ [18,19]	$\sigma(0)\simeq 2$ [18,19]	$\sigma(0)\to 0$ for $h\to 1$ [18,19]
FM/I/S	U (V) shape [12,17,57]	No ZBCP for $h\geqslant 1$ [13–17]	ZBCP [18,19]	ZBCP [18,19]	No ZBCP for $h\geqslant 1$ [18,19]
ARM/S	$\sigma(0)>0$ for $\alpha>0$	$\sigma(0)>0$ for $\alpha>0$	$\sigma(0)=0$ for $\alpha>0$	$\sigma(0)\simeq 2$	$\sigma(0)=0$
ARM/I/S	U (V) shape	ZBCP for $\alpha>0$	No ZBCP	ZBCP	No ZBCP

superconductor junctions [8] [see Fig. 17(B)(a)]. However, for FM/helical p-waves, the broad ZBCP remains even for $h>1.0$ since, in those cases, the direction of the $\boldsymbol{d}$ vector is in the xy plane [18,19] [see Fig. 17(B)(b)]. On the other hand, for ARM/helical p-waves, $\sigma(|eV|<\Delta_0)$ is not seriously suppressed and has a small dip around zero-bias voltage [61], as shown in Fig. 17(B)(c). In addition, the dip gets bigger as the magnitude of the RSOI increases. This feature is different from that in the ARM/chiral p-wave superconductor junction.

Finally, we calculate $\sigma(eV)$ for chiral d-wave junctions where the time-reversal symmetry is broken, similar to the case of chiral p-wave pairing. f_{θ_S} is given by

$$f_{\theta_S}=\exp(2i\theta_S). \tag{44}$$

For N/chiral d-waves, $\sigma(eV)$ has an almost flat line shape as a function of bias voltage [62]. Although two branches of the SABS exist, they do not cross $E=0$ at $k_y=0$, in contrast to the chiral p-wave and helical p-wave pairing cases. Then, the contribution from $E=0$ is not large and the resulting $\sigma(eV)$ does not have a ZBCP [see Fig. 17(C)(a)] [62]. When we consider FM/chiral d-waves, $\sigma(|eV|<\Delta_0)$ is reduced with the increase in the magnitude of the exchange field since chiral d-wave symmetry belongs to a spin-singlet pairing. In particular, $\sigma(eV=0)=0$ is satisfied in the junction with the FPFM [see Fig. 17(C)(b)(iii)]. Similar to $\sigma(|eV|<\Delta_0)$ in the ARM/spin-singlets shown in the previous section, that in ARM/chiral d-waves is enhanced with the increase of the magnitude of the RSOI [see Fig. 17(C)(c)].

As a summary of the results, if we consider only the N/S junctions, it is difficult to distinguish between chiral p-wave and helical p-wave pairings [7,8,62]. For the FM/S junctions with a sufficiently large magnitude of spin polarization, it is also difficult to distinguish the chiral d-wave from the chiral p-wave [18,19,62]. However, for the ARM/S junctions, the qualitative line shapes of $\sigma(eV)$ have a different feature for each pairing. Therefore, the ARM is useful to classify three pairings that have the SABS with linear dispersions. The behavior of the tunneling conductance is summarized in Table I.

V. CONCLUSION

In this paper, we have theoretically studied tunneling conductance between ARM/S junctions for various types of the pairing symmetry in S. For the ARM/spin-singlet superconductor junction, the magnitude of the inner gap conductance is enhanced as compared to that in the FPFM junction. It is noted that the ZBCP recovers in the ARM/d_{xy}-wave superconductor junction by the RSOI while it is completely suppressed in the FPFM/d_{xy}-wave superconductor junction. In a previous work [51], the anomalous behavior of the conductance in LSMO/YBCO junctions was not reported, and its origin has not been discovered. Our obtained results can explain the ZBCP in LSMO/YBCO junctions in the presence of the large magnitude of the exchange field. Due to the absence of inversion symmetry, RSOI is induced near the interface of LSMO. Therefore, it is natural to speculate that LSMO can behave like the ARM near the interface. Based on this, the robust ZBCP reported in LSMO/YBCO junctions seems to be reasonable [51].

We have also studied tunneling conductance in ARM/p_x-wave superconductor junctions. It has been revealed that whether the ZBCP remains or not depends critically on the direction of the $\boldsymbol{d}$-vector in ARM/p_x-wave superconductor junctions, and this can be understood by using the winding number W. In addition, we have calculated the tunneling conductance in the ARM/S junction, where the symmetry of S is the chiral p-wave, helical p-wave, and chiral d-wave pairings. We have shown that these three types of pairings show qualitatively different line shapes of tunneling conductance. Our obtained results are useful to determine the pairing symmetry of the superconductor Sr_2RuO_4.

In this paper, we have focused on the quasiparticle tunneling in ARM/S junctions. It is a challenging problem to study Josephson current in S/ARM/S junctions since an SABS [4,63] seriously influences the magnitude of Josephson current at low temperatures. Although a theoretical study on N/S or S/N/S junctions in the presence of RSOI in N was performed in some recent work [64,65], the Josephson current in an S/ARM/S junction has not been revealed specifically for unconventional superconductors as of yet. We are planning to study this issue in the near future.

ACKNOWLEDGMENTS

This work was supported by a Grant-in Aid for Scientific Research on Innovative Areas "Topological Material Science" (Grant No. 15H05853), a Grant-in-Aid for Scientific Research B (Grant No. 15H03686), a Grant-in-Aid for Challenging Exploratory Research (Grant No. 15K13498), and a Grant-in-Aid for JSPS Fellows (Grants No. 13J06466 and No. 13J03141) (S.K. and K.T.).

APPENDIX A: WINDING NUMBER IN p_x-WAVE SUPERCONDUCTORS

We discuss here the winding number of p_x-wave superconductors of the one-dimensional limit, which guarantees the existence of a Majorana edge state and complements our numerical results. We start from the BdG Hamiltonian of a one-dimensional p_x-wave superconductor,

$$\bar{H}_{\rm BdG}(k_x) = [2t\cos(k_x) - \mu]\hat{\sigma}_0\hat{\tau}_z + \bar{\Delta}(k_x), \tag{A1}$$

with

$$\bar{\Delta}(k_x) = \begin{cases} -\Delta_0 \sin k_x \hat{\sigma}_z\hat{\tau}_x & (\boldsymbol{d} \parallel \boldsymbol{x}), \\ \Delta_0 \sin k_x \hat{\sigma}_0\hat{\tau}_y & (\boldsymbol{d} \parallel \boldsymbol{y}), \\ \Delta_0 \sin k_x \hat{\sigma}_x\hat{\tau}_x & (\boldsymbol{d} \parallel \boldsymbol{z}), \end{cases} \tag{A2}$$

where μ is the chemical potential and Δ_0 is the amplitude of the gap function. $\hat{\sigma}_i$ ($\hat{\tau}_i$) ($i = 0,x,y,z$) are the identity matrix and the Pauli matrices in the spin (Nambu) space. This system satisfies the time-reversal symmetry $\bar{T}\bar{H}_{\rm BdG}(k_x)\bar{T}^{-1} = \bar{H}_{\rm BdG}(-k_x)$ and the particle-hole symmetry $\bar{C}\bar{H}_{\rm BdG}(k_x)\bar{C}^{-1} = -\bar{H}_{\rm BdG}(-k_x)$ by $\bar{T} = i\hat{\sigma}_y\hat{\tau}_0 K$ and $\bar{C} = \hat{\sigma}_0\hat{\tau}_x K$, where K is the complex conjugation.

If the BdG Hamiltonian has a chiral operator $\bar{\Gamma}$, i.e., $\{\bar{\Gamma}, \bar{H}_{\rm BdG}(k_x)\} = 0$, then the winding number is defined by [52,66–68]

$$W \equiv \frac{-1}{4\pi i}\int_{-\pi}^{\pi} dk_x \,{\rm Tr}\left[\bar{\Gamma}\bar{H}_{\rm BdG}(k_x)^{-1}\partial_{k_x}\bar{H}_{\rm BdG}(k_x)\right], \tag{A3}$$

which takes an integer. In time-reversal invariant superconductors, the combination of time-reversal operator $\bar{T}$ and particle-hole operator $\bar{C}$ becomes the chiral operator $\bar{\Gamma}_0 = -i\bar{C}\bar{T}$. Due to inversion symmetry, we notice that whereas Eq. (A3) with $\bar{\Gamma}_0$ yields a nontrivial winding number in spin-singlet superconductors, it leads to $W = 0$ in spin-triplet superconductors [53,69]. Thus, in order to pursue a nontrivial winding number in a spin-triplet pairing, we require the help of material-dependent symmetries in addition to $\bar{T}$ and $\bar{C}$.

Equation (A1) possesses spin-rotational symmetries: $\bar{U}_x = i\hat{\sigma}_x\hat{\tau}_z$, $\bar{U}_y = -i\hat{\sigma}_y\hat{\tau}_0$, and $\bar{U}_z = i\hat{\sigma}_z\hat{\tau}_z$, which satisfy $[\bar{U}_i, \bar{H}_{\rm BdG}(k_x)] = 0$ when the $\boldsymbol{d}$ vector is parallel to the i direction. Taking into account this additional symmetry, we can define a spin-dependent chiral operator $\bar{\Gamma}_i \equiv \bar{C}\bar{T}\bar{U}_i$, and Eq. (A3) with $\bar{\Gamma}_i$ leads, for each direction of the $\boldsymbol{d}$ vector, to

$$W = \begin{cases} 2, & 0 < \mu < 2t, \\ 0 & \text{otherwise}, \end{cases} \tag{A4}$$

where $W = 2$ indicates the presence of a Majorana Kramer's pair at both ends.

On the other hand, in our numerical result, we found that the zero-bias conductance peak is suppressed when $\boldsymbol{d} \parallel \boldsymbol{x}$ and $\boldsymbol{d} \parallel z$. To explain this suppression from Eq. (A4), we consider how the Rashba spin-orbit interaction (RSOI) and the exchange field affect the Majorana Kramer's pair by adding the terms

$$\bar{H}' = \lambda \sin k_x \hat{\sigma}_y\hat{\tau}_z + H\hat{\sigma}_z\hat{\tau}_z \tag{A5}$$

into the BdG Hamiltonian, where the parameters λ and H indicate the amplitude of RSOI and the exchange field, respectively. We readily find that the first term breaks the spin-rotational symmetries $\bar{U}_x$ and $\bar{U}_z$, i.e., the winding number survives only when $\boldsymbol{d} \parallel \boldsymbol{y}$. In addition, although a Majorana Kramer's pair is fragile against the exchange effect, we have the effective time-reversal symmetry $\bar{T}' = \bar{T}\bar{U}_y$ for the y direction, which keeps the Majorana Kramer's pair intact even when the Zeeman effect is present [70,71]. As a result, the topological argument is consistent with our calculation of the tunneling conductance.

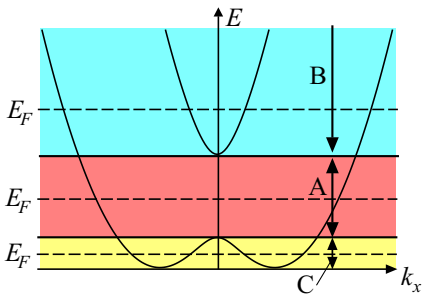

FIG. 18. (Color online) Energy spectrum of the Rashba metal with exchange field. There are three regions A, B, and C, depending on μ.

APPENDIX B: FORMULATION FOR THE TUNNELING CONDUCTANCE IN RASHBA METAL WITH EXCHANGE FIELD/SUPERCONDUCTOR JUNCTIONS

We show here formulations for the tunneling conductance of Rashba metal (RM)/insulator/superconductor junctions in the presence of the exchange field in the RM where the number of Fermi surfaces is two. The BdG Hamiltonian of this system is already given by Eqs. (1)–(3). In this Appendix, we shift attention from the ARM ($|\mu| < H$) to the RM ($|\mu| > H$) and derive the wave functions for $x < 0$ and the tunneling conductance. Therefore, the wave functions for $x < 0$ and the tunneling conductance are mainly introduced in this appendix. If we choose $H = 0$, the resulting tunneling conductance corresponds with that shown in Sec. III C (see Fig. 14).

The dispersion in the RM with the exchange field is shown in Fig. 18. From Fig. 18, it is found that we can define three regions (A, B, and C) depending on the parameters: H, λ, and

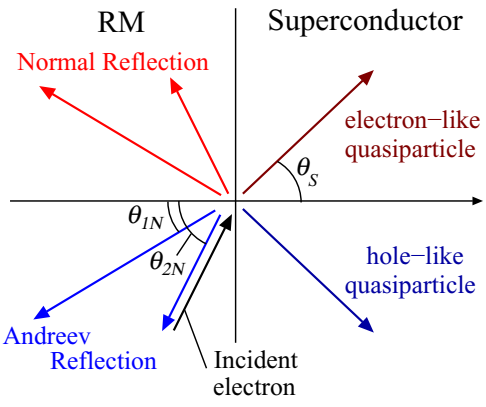

FIG. 19. (Color online) Schematic illustration of the scattering process. $\theta_{1(2)N}$ is an incident angle of an electron with momentum $k_{1(2)}$ with respect to the interface normal. θ_S denotes the direction of motions of quasiparticles in S measured from the interface normal.

μ_N. The ARM is realized in region A with $|\mu| < H$. On the other hand, the RM is realized in region B (C) with $\mu > H$ ($-\frac{(m\lambda)^2+H^2}{2(m\lambda)^2} < \mu < -H$). In regions B and C we have two Fermi surfaces, unlike in region A. Thus, we need to take into account the inner Fermi surface in addition to the outer Fermi surface. Interestingly, the inner and outer Fermi surfaces have different helicity from each other in region B while they have the same spin helicity in region C. The scattering process for regions B and C is shown in Fig. 19. θ_{1N} (θ_{2N}) is an incident angle of momentum for the outer (inner) Fermi surface k_1 (k_2). The momenta correspond to what we have shown in Sec. II:

$$k_1 = \sqrt{2m(\mu_N + m\lambda^2 + \sqrt{(m\lambda^2)^2 + 2m\lambda^2\mu_N + H^2})}, \quad k_2 = \sqrt{2m(\mu_N + m\lambda^2 - \sqrt{(m\lambda^2)^2 + 2m\lambda^2\mu_N + H^2})},$$

and the y component of all momenta is given by

$$k_y = k_1 \sin\theta_{1N} = k_2 \sin\theta_{2N} = k_S \sin\theta_S. \tag{B1}$$

In what follows, we discuss the formulations in regions B (i) and C (ii).

(i) In this paragraph, we show the formulation for the tunneling conductance of a two-dimensional RM with the exchange field (region B)/insulator/superconductor junction. The wave functions are represented by using the eigenfunctions of the BdG Hamiltonian for $\mu > H$. First, we introduce the wave function in the case in which an electron of the outer Fermi surface injects,

$$\begin{aligned}\psi(x<0,y) = \frac{1}{\sqrt{2}}e^{ik_y y}\Bigg(& e^{ik_1\cos\theta_{1N}x}\begin{bmatrix} s \\ 1 \\ 0 \\ 0 \end{bmatrix} + r_{1(2)}e^{-ik_1\cos\theta_{1N}x}\begin{bmatrix} s^* \\ 1 \\ 0 \\ 0 \end{bmatrix} + a_{1(2)}e^{ik_1\cos\theta_{1N}x}\begin{bmatrix} 0 \\ 0 \\ -s^* \\ 1 \end{bmatrix} \\ & + r_{2(1)}e^{-iK_{eBx}x}\begin{bmatrix} t_{B1e} \\ 1 \\ 0 \\ 0 \end{bmatrix} + a_{2(1)}e^{iK_{hBx}x}\begin{bmatrix} 0 \\ 0 \\ -t_{B1h} \\ 1 \end{bmatrix}\Bigg), \\ s = -\frac{i\lambda k_1 e^{-i\theta_{1N}}}{\xi_{k_1}+H}&, \\ t_{B1e(h)} = -\frac{\lambda(-iK_{e(h)Bx}+k_y)}{\xi_{k_2}+H}&, \\ K_{e(h)Bx} = \begin{cases} k_2\cos\theta_{2N} & (k_1\sin\theta_{1N} < k_2), \\ +(-)i\sqrt{(k_1)^2\sin^2\theta_{1N} - (k_2)^2} & (k_1\sin\theta_{1N} > k_2). \end{cases}\end{aligned} \tag{B2}$$

For $k_1 \sin\theta_{1N} > k_2$, the normal and Andreev reflections from the inner Fermi surface become evanescent waves. Next, we introduce the wave function in the case in which an electron of the inner Fermi surface injects,

$$\begin{aligned}\psi(x<0,y) = \frac{1}{\sqrt{2}}e^{ik_y y}\Bigg(& e^{ik_2\cos\theta_{2N}x}\begin{bmatrix} t_{B2} \\ 1 \\ 0 \\ 0 \end{bmatrix} + r_1 e^{-ik_1\cos\theta_{1N}x}\begin{bmatrix} s^* \\ 1 \\ 0 \\ 0 \end{bmatrix} + a_1 e^{ik_1\cos\theta_{1N}x}\begin{bmatrix} 0 \\ 0 \\ -s^* \\ 1 \end{bmatrix} \\ & + r_2 e^{-ik_2\cos\theta_{2N}x}\begin{bmatrix} t^*_{B2} \\ 1 \\ 0 \\ 0 \end{bmatrix} + a_2 e^{ik_2\cos\theta_{2N}x}\begin{bmatrix} 0 \\ 0 \\ -t^*_{B2} \\ 1 \end{bmatrix}\Bigg), \\ s = -\frac{i\lambda k_1 e^{-i\theta_{1N}}}{\xi_{k_1}+H}&, \\ t_{B2} = -\frac{i\lambda k_2 e^{-i\theta_{2N}}}{\xi_{k_2}+H}&.\end{aligned} \tag{B3}$$

We assume that the wave function in the junction satisfies the boundary condition given by Eq. (26). The obtained tunneling conductance is given as follows:

$$\sigma(E) = \frac{1}{2}\sigma_1(E) + \frac{1}{2}\sigma_2(E), \tag{B4}$$

$$\sigma_1(E) = \frac{\int \sigma_{1S}(E,\theta_S)d\theta_S}{\int \sigma_{1N}(E,\theta_S)d\theta_S}, \tag{B5}$$

$$\sigma_2(E) = \frac{\int \sigma_{2S}(E,\theta_S)d\theta_S}{\int \sigma_{2N}(E,\theta_S)d\theta_S}. \tag{B6}$$

Here, $\sigma_{1\,(2)}(E)$ means normalized tunneling conductance when an electron from the outer (inner) Fermi surface injects. In addition, σ_{iS} (σ_{iN}) represents tunneling conductance between the ARM/S [the ARM/normal metal ($\Delta_0 = 0$)] junction, where $i = 1,2$. In Eqs. (B5) and (B6), $\sigma_{1S}(E,\theta_S)$ and $\sigma_{2S}(E,\theta_S)$ are given by

$$\sigma_{1S}(E,\theta_S) = \begin{cases} 4e\Big((1+|a_1|^2-|r_1|^2)\Big(\frac{k_1\cos\theta_{1N}}{m}(|s|^2+1)-i\lambda(s-s^*)\Big) \\ \quad +(|a_2|^2-|r_2|^2)\Big(\frac{k_2\cos\theta_{2N}}{m}(|t_{B1e}|^2+1)+i\lambda(t_{B1e}-t_{B1e}^*)\Big)\Big) & (k_1\sin\theta_{1N} < k_2), \\ 4e(1+|a_1|^2-|r_1|^2)\Big(\frac{k_1\cos\theta_{1N}}{m}(|s|^2+1)-i\lambda(s-s^*)\Big) & (k_1\sin\theta_{1N} > k_2), \end{cases} \tag{B7}$$

$$\sigma_{2S}(E,\theta_S) = 4e\Bigg[(1+|a_2|^2-|r_2|^2)\Big(\frac{k_2\cos\theta_{2N}}{m}(|t_{B2}|^2+1)-i\lambda(t_{B2}-t_{B2}^*)\Big) + (|a_1|^2-|r_1|^2)\Big(\frac{k_1\cos\theta_{1N}}{m}(|s|^2+1)-i\lambda(s-s^*)\Big)\Bigg]. \tag{B8}$$

(ii) Next, we show the formulation for the tunneling conductance of a two-dimensional RM with the exchange field (region C)/insulator/superconductor junction. Wave functions are represented by using the eigenfunctions of the BdG Hamiltonian for $-\frac{(m\lambda)^2+H^2}{2(m\lambda)^2} < \mu < -H$. First, we introduce the wave function in the case in which an electron of the outer Fermi surface injects,

$$\psi(x,y) = \frac{1}{\sqrt{2}}e^{ik_y y}\Bigg(e^{ik_1\cos\theta_{1N}x}\begin{bmatrix}s\\1\\0\\0\end{bmatrix} + r_1 e^{-ik_1\cos\theta_{1N}x}\begin{bmatrix}s^*\\1\\0\\0\end{bmatrix} + a_1 e^{ik_1\cos\theta_{1N}x}\begin{bmatrix}0\\0\\-s^*\\1\end{bmatrix} + r_2 e^{-iK_{2ex}x}\begin{bmatrix}t_{C1e}\\1\\0\\0\end{bmatrix} + a_2 e^{iK_{2hx}x}\begin{bmatrix}0\\0\\-t_{C1h}\\1\end{bmatrix}\Bigg),$$

$$s = -\frac{i\lambda k_1 e^{-i\theta_{1N}}}{\xi_{\boldsymbol{k}_1}+H}, \qquad t_{C1e(h)} = -\frac{\lambda(iK_{e(h)Cx}+k_y)}{\xi_{\boldsymbol{k}_2}+H}, \qquad K_{2e(h)x} = \begin{cases} k_2\cos\theta_{2N} & (k_1\sin\theta_{1N} < k_2), \\ +(-)i\sqrt{(k_1)^2\sin^2\theta_{1N}-k_2^2} & (k_1\sin\theta_{1N} > k_2). \end{cases} \tag{B9}$$

For $k_1\sin\theta_{1N} > k_2$, the normal and Andreev reflections from the inner Fermi surface become evanescent waves. Next, we introduce the wave function in the case in which an electron of the inner Fermi surface injects,

$$\psi(x,y) = \frac{1}{\sqrt{2}}e^{ik_y y}\Bigg(e^{ik_2\cos\theta_{2N}x}\begin{bmatrix}t_{C2}^*\\1\\0\\0\end{bmatrix} + r_1 e^{-ik_1\cos\theta_{1N}x}\begin{bmatrix}s^*\\1\\0\\0\end{bmatrix} + a_1 e^{ik_1\cos\theta_{1N}x}\begin{bmatrix}0\\0\\-s^*\\1\end{bmatrix} + r_2 e^{-ik_2\cos\theta_{2N}x}\begin{bmatrix}t_{C2}\\1\\0\\0\end{bmatrix} + a_2 e^{ik_2\cos\theta_{2N}x}\begin{bmatrix}0\\0\\-t_{C2}\\1\end{bmatrix}\Bigg),$$

$$s = -\frac{i\lambda k_1 e^{-i\theta_{1N}}}{\xi_{\boldsymbol{k}_1}+H}, \qquad t_{C2} = -\frac{i\lambda k_2 e^{-i\theta_{2N}}}{\xi_{\boldsymbol{k}_2}+H}. \tag{B10}$$

We assume that the wave function satisfies the boundary condition given by Eq. (26). The obtained tunneling conductance is given as follows:

$$\sigma(E) = \frac{1}{2}\sigma_1(E) + \frac{1}{2}\sigma_2(E), \tag{B11}$$

$$\sigma_1(E) = \frac{\int\sigma_{1S}(E,\theta_S)d\theta_S}{\int\sigma_{1N}(E,\theta_S)d\theta_S}, \tag{B12}$$

$$\sigma_2(E) = \frac{\int\sigma_{2S}(E,\theta_S)d\theta_S}{\int\sigma_{2N}(E,\theta_S)d\theta_S}. \tag{B13}$$

Here, $\sigma_{1\,(2)}(E)$ means normalized tunneling conductance when an electron from the outer (inner) Fermi surface injects. In addition, σ_{iS} (σ_{iN}) represents tunneling conductance between the ARM/S [the ARM/normal metal ($\Delta_0 = 0$)] junction, where

$i = 1,2$. In Eqs. (B12) and (B13), $\sigma_{1S}(E,\theta_S)$ and $\sigma_{2S}(E,\theta_S)$ are given by

$$\sigma_{1S}(E,\theta_S) = \begin{cases} 4e\Big((1+|a_1|^2-|r_1|^2)\Big(\frac{k_1\cos\theta_{1N}}{m}(|s|^2+1)-i\lambda(s-s^*)\Big) \\ \quad +(|a_2|^2-|r_2|^2)\Big(\frac{k_2\cos\theta_{2N}}{m}(|t_{C1e}|^2+1)-i\lambda(t_{C1e}-t_{C1e}^*)\Big)\Big) & (k_1\sin\theta_{1N} < k_2), \\ 4e(1+|a_1|^2-|r_1|^2)\Big(\frac{k_1\cos\theta_{1N}}{m}(|s|^2+1)-i\lambda(s-s^*)\Big) & (k_1\sin\theta_{1N} > k_2), \end{cases} \tag{B14}$$

$$\sigma_{2S}(E,\theta_S) = 4e\Bigg[(1+|a_2|^2-|r_2|^2)\Big(\frac{k_2\cos\theta_{2N}}{m}(|t_{C2}|^2+1)-i\lambda(t_{C2}-t_{C2}^*)\Big) + (|a_1|^2-|r_1|^2)\Big(\frac{k_1\cos\theta_{1N}}{m}(|s|^2+1)-i\lambda(s-s^*)\Big)\Bigg]. \tag{B15}$$

[1] L. J. Buchholtz and G. Zwicknagl, Phys. Rev. B **23**, 5788 (1981).
[2] J. Hara and K. Nagai, Prog. Theor. Phys. **76**, 1237 (1986).
[3] C. R. Hu, Phys. Rev. Lett. **72**, 1526 (1994).
[4] S. Kashiwaya and Y. Tanaka, Rep. Prog. Phys. **63**, 1641 (2000).
[5] Y. Tanaka and S. Kashiwaya, Phys. Rev. Lett. **74**, 3451 (1995).
[6] T. Löfwander, V. S. Shumeiko, and G. Wendin, Supercond. Sci. Technol. **14**, R53 (2001); S. Kashiwaya, Y. Tanaka, N. Terada, M. Koyanagi, S. Ueno, L. Alff, H. Takashima, Y. Tanuma, and K. Kajimura, J. Phys. Chem. Solids **59**, 2034 (1998); M. Covington, M. Aprili, E. Paraoanu, L. H. Greene, F. Xu, J. Zhu, and C. A. Mirkin, Phys. Rev. Lett. **79**, 277 (1997); L. Alff, H. Takashima, S. Kashiwaya, N. Terada, H. Ihara, Y. Tanaka, M. Koyanagi, and K. Kajimura, Phys. Rev. B **55**, R14757(R) (1997); J. Y. T. Wei, N.-C. Yeh, D. F. Garrigus, and M. Strasik, Phys. Rev. Lett. **81**, 2542 (1998); I. Iguchi, W. Wang, M. Yamazaki, Y. Tanaka, and S. Kashiwaya, Phys. Rev. B **62**, R6131(R) (2000); A. Biswas, P. Fournier, M. M. Qazilbash, V. N. Smolyaninova, H. Balci, and R. L. Greene, Phys. Rev. Lett. **88**, 207004 (2002); B. Chesca, H. J. H. Smilde, and H. Hilgenkamp, Phys. Rev. B **77**, 184510 (2008).
[7] S. Kashiwaya, H. Kashiwaya, H. Kambara, T. Furuta, H. Yaguchi, Y. Tanaka, and Y. Maeno, Phys. Rev. Lett. **107**, 077003 (2011).
[8] M. Yamashiro, Y. Tanaka, and S. Kashiwaya, Phys. Rev. B **56**, 7847 (1997).
[9] M. Yamashiro, Y. Tanaka, Y. Tanuma, and S. Kashiwaya, J. Phys. Soc. Jpn. **67**, 3224 (1998).
[10] C. Honerkamp and M. Sigrist, J. Low Temp. Phys. **111**, 895 (1998).
[11] C. Iniotakis, N. Hayashi, Y. Sawa, T. Yokoyama, U. May, Y. Tanaka, and M. Sigrist, Phys. Rev. B **76**, 012501 (2007).
[12] M. J. M. de Jong and C. W. J. Beenakker, Phys. Rev. Lett. **74**, 1657 (1995).
[13] S. Kashiwaya, Y. Tanaka, N. Yoshida, and M. R. Beasley, Phys. Rev. B **60**, 3572 (1999).
[14] I. Žutić and S. Das Sarma, Phys. Rev. B **60**, R16322 (1999).
[15] I. Žutić and O. T. Valls, Phys. Rev. B **61**, 1555 (2000).
[16] J.-X. Zhu and C. S. Ting, Phys. Rev. B **61**, 1456 (2000).
[17] J. Linder, M. Cuoco, and A. Sudbø, Phys. Rev. B **81**, 174526 (2010).
[18] Y. Tanaka, T. Hirai, K. Kusakabe, and S. Kashiwaya, Phys. Rev. B **60**, 6308 (1999).
[19] T. Hirai, Y. Tanaka, N. Yoshida, Y. Asano, J. Inoue, and S. Kashiwaya, Phys. Rev. B **67**, 174501 (2003).
[20] E. Rashba, Sov. Phys. Solid. State **2**, 1109 (1960).
[21] Y. A. Bychkov and E. I. Rashba, JETP Lett. **2**, 78 (1984).
[22] L. W. Molenkamp, G. Schmidt, and G. E. W. Bauer, Phys. Rev. B **64**, 121202 (2001).
[23] P. Středa and P. Šeba, Phys. Rev. Lett. **90**, 256601 (2003).
[24] L. Jin, L. Zhu, X. Zhou, L. Li, and Z.-W. Xie, J. Appl. Phys. **107**, 103722 (2010).
[25] T. Kato, Y. Ishikawa, H. Itoh, and J.-i. Inoue, Phys. Rev. B **77**, 233404 (2008).
[26] D. Grundler, Phys. Rev. Lett. **86**, 1058 (2001).
[27] B. Srisongmuang, P. Pairor, and M. Berciu, Phys. Rev. B **78**, 155317 (2008).
[28] T. Yokoyama, Y. Tanaka, and J. Inoue, Phys. Rev. B **74**, 035318 (2006).
[29] Y. Mizuno, T. Yokoyama, and Y. Tanaka, Phys. Rev. B **80**, 195307 (2009).
[30] K. Sun and N. Shah, Phys. Rev. B **91**, 144508 (2015).
[31] I. Miron, G. Gaudin, S. Auffret, B. Rodmacq, A. Schuhl, S. Pizzini, J. Vogel, and P. Gambardella, Nat. Mater. **9**, 230 (2010).
[32] M. Z. Hasan and C. L. Kane, Rev. Mod. Phys. **82**, 3045 (2010).
[33] P. Schwab, R. Raimondi, and C. Gorini, Europhys. Lett. **93**, 67004 (2011).
[34] L. Fu and C. L. Kane, Phys. Rev. Lett. **100**, 096407 (2008).
[35] A. R. Akhmerov, J. Nilsson, and C. W. J. Beenakker, Phys. Rev. Lett. **102**, 216404 (2009).
[36] K. T. Law, P. A. Lee, and T. K. Ng, Phys. Rev. Lett. **103**, 237001 (2009).
[37] Y. Tanaka, T. Yokoyama, and N. Nagaosa, Phys. Rev. Lett. **103**, 107002 (2009).
[38] J. Linder, Y. Tanaka, T. Yokoyama, A. Sudbo, and N. Nagaosa, Phys. Rev. Lett. **104**, 067001 (2010).
[39] J. Alicea, Phys. Rev. B **81**, 125318 (2010).
[40] J. D. Sau, R. M. Lutchyn, S. Tewari, and S. Das Sarma, Phys. Rev. Lett. **104**, 040502 (2010).
[41] M. Sato, Y. Takahashi, and S. Fujimoto, Phys. Rev. Lett. **103**, 020401 (2009).
[42] M. Sato, Y. Takahashi, and S. Fujimoto, Phys. Rev. B **82**, 134521 (2010).
[43] R. M. Lutchyn, J. D. Sau, and S. Das Sarma, Phys. Rev. Lett. **105**, 077001 (2010).
[44] Y. Oreg, G. Refael, and F. von Oppen, Phys. Rev. Lett. **105**, 177002 (2010).
[45] A. Yamakage, Y. Tanaka, and N. Nagaosa, Phys. Rev. Lett. **108**, 087003 (2012).

[46] AF. Andreev, Sov. Phys. JETP **19**, 1228 (1964).
[47] G. E. Blonder, M. Tinkham, and T. M. Klapwijk, Phys. Rev. B **25**, 4515 (1982).
[48] B. Béri, Phys. Rev. B **79**, 245315 (2009).
[49] P. A. Ioselevich and M. V. Feigel'man, New J. Phys. **15**, 055011 (2013).
[50] P. San-Jose, J. Cayao, E. Prada, and R. Aguado, arXiv:1409.7306.
[51] H. Kashiwaya, S. Kashiwaya, B. Prijamboedi, A. Sawa, I. Kurosawa, Y. Tanaka, and I. Iguchi, Phys. Rev. B **70**, 094501 (2004).
[52] M. Sato, Y. Tanaka, K. Yada, and T. Yokoyama, Phys. Rev. B **83**, 224511 (2011).
[53] S. Kobayashi, K. Shiozaki, Y. Tanaka, and M. Sato, Phys. Rev. B **90**, 024516 (2014).
[54] K. Sengupta, I. Žutić, H.-J. Kwon, V. M. Yakovenko, and S. Das Sarma, Phys. Rev. B **63**, 144531 (2001).
[55] Y. Tanaka, Y. Tanuma, K. Kuroki, and S. Kashiwaya, J. Phys. Soc. Jpn. **71**, 2102 (2002).
[56] J. Bardeen, Phys. Rev. Lett. **6**, 57 (1961).
[57] R. Merservey and P. Tedrow, Phys. Rep. **238**, 173 (1994).
[58] Y. Maeno, S. Kittaka, T. Nomura, S. Yonezawa, and K. Ishida, J. Phys. Soc. Jpn. **81**, 011009 (2012).
[59] Y. Tada, N. Kawakami, and S. Fujimoto, New J. Phys. **11**, 055070 (2009).
[60] Y. Ueno, A. Yamakage, Y. Tanaka, and M. Sato, Phys. Rev. Lett. **111**, 087002 (2013).
[61] S. P. Mukherjee, Eur. Phys. B **80**, 51 (2011).
[62] S. Kashiwaya, H. Kashiwaya, K. Saitoh, Y. Mawatari, and Y. Tanaka, Physica E **55**, 25 (2014).
[63] Y. Tanaka and S. Kashiwaya, Phys. Rev. B **56**, 892 (1997).
[64] T. Yokoyama, M. Eto, and Y. V. Nazarov, Phys. Rev. B **89**, 195407 (2014).
[65] J. Cayao, E. Prada, P. San-Jose, and R. Aguado, Phys. Rev. B **91**, 024514 (2015).
[66] X. G. Wen and A. Zee, Phys. Rev. B **66**, 235110 (2002).
[67] B. Béri, Phys. Rev. B **81**, 134515 (2010).
[68] A. P. Schnyder and S. Ryu, Phys. Rev. B **84**, 060504 (2011).
[69] S. Kobayashi, Y. Tanaka, M. Sato, arXiv:1510.01411.
[70] E. Dumitrescu and S. Tewari, Phys. Rev. B **88**, 220505 (2013).
[71] E. Dumitrescu, J. D. Sau, and S. Tewari, Phys. Rev. B **90**, 245438 (2014).